

THESIS TITLE
SECOND LINE IF NECESSARY

by

DILRAJ GHUMAN

A thesis submitted to the
Department of Physics, Engineering Physics and Astronomy
in conformity with the requirements for
the degree of Master of Science

Queen's University
Kingston, Ontario, Canada

July 2021

Copyright © Dilraj Ghuman, 2021

Abstract

This is my abstract.

Acknowledgments

Blah blah blah.

Statement of Originality

Contents

Abstract	i
Acknowledgments	ii
Statement of Originality	iii
Contents	iv
List of Tables	vi
List of Figures	vii
Chapter 1: Introduction	1
Chapter 2: Background	2
2.1 Neutrinos	2
2.1.1 Oscillations	2
2.1.2 Interactions	7
2.1.3 Solar Production	9
2.1.4 Atmospheric Production	9
2.1.5 Geological Production	10
2.1.6 Reactor Production	10
2.1.7 Accelerator Production	11
2.1.8 Galactic Production	11
2.2 Detection Techniques	12
2.2.1 Germanium Detectors	12
2.2.2 Calorimeters	12
2.2.3 Vavilov–Cherenkov	13
2.3 Neutrino Telescopes	14
2.3.1 IceCube	14
2.3.2 ANTARES	16
2.3.3 KM3NET	17

Chapter 3: The Pacific Ocean Neutrino Explorer	18
3.1 Geometry	18
3.2 Detectors	19
3.2.1 Photomultiplier Tubes	20
3.2.2 Digital Optical Modules	21
3.2.3 mDOMs	22
3.3 Strings for Absorption length in Water	22
3.4 Ocean Networks Canada	24
Chapter 4: Simulation	27
4.1 IceCube Framework	27
4.2 Simulating Neutrinos	28
4.3 Simulating Muons	28
4.4 Detector Response	29
Chapter 5: Reconstruction	31
5.1 Geometry of a Single Hit	31
5.2 Linefit	37
5.3 Likelihood	38
5.3.1 Likelihood Function	39
5.3.2 Function Fitting	44
5.3.3 Other Potential Distributions	46
5.4 Track Fitting	51
5.5 Corrections	52
5.5.1 Reparameterizing	52
5.5.2 Extra Penalty	53
Chapter 6: Results	54
6.1 Linefit	54
6.2 Likelihood	55
Chapter 7: Summary and Conclusions	68
7.1 Summary	68
7.2 Future Work	68
7.3 Conclusion	68
Bibliography	69

List of Tables

- | | |
|--|----|
| 6.1 Some simple statistics on the data distributions in Figure 6.3. Here ‘line’, ‘default’ and ‘true’ refer to just the linear fit, the likelihood using the linear fit as the seed, and the likelihood using the truth as a seed fits respectively. The means (μ) are computed in the standard way, but the standard deviation (σ_s) is the sample standard deviation, and hence is normalized by a factor dependent upon the sample size. | 58 |
| 6.2 The labels ‘line’, ‘llh’, ‘llhdir’, ‘llhvvert’, ‘llhtrue’ refer to the linefit, likelihood, likelihood using the true direction seed, likelihood using the true vertex seed and likelihood using the truth as a seed reconstructions respectively. The values are given in percentage of events below the given α solid angle to the true direction. | 61 |

List of Figures

2.1	The Feynmann diagrams for the vertices that would be included in neutrino interactions using the charged W^\pm boson on the left and the neutral Z^0 boson on the right.	8
3.1	Left: Proposed full detector of the P–ONE detector. Right: Proposed array for the Explorer deployment of P–ONE.	19
3.2	A diagram and schematic of the IceCube DOM.	21
3.3	A diagram of the full STRAW setup including distances [15].	23
3.4	A diagram of the Ocean Networks Canada Western Infrastructure for monitoring the Pacific Ocean. This contains the NEPTUNE and VENUS observatories. Source [2].	25
3.5	Diagram of the Cascadia Basin, the site of the upcoming P–ONE experiment and current site of the pathfinder STRAW. Source [2]. . .	26
5.1	Drawing of muon track and Vavilov-Cherenkov Radiation hitting a single DOM where \vec{r}_i is the DOM location, \vec{q}_i is the emission point of the photon, and d_i is the distance the photon travels to the DOM. . .	32

5.2	Drawing of a track with vertex and DOM labeled. The origin here is also marked to emphasize the vector notation and algebra. It is easy enough to see the vector algebra required to get the distance of closest approach through this diagram.	35
5.3	Upward Arrival Time	36
5.4	Downward Arrival Time	36
5.5	Drawing of the position and time space with possible points (x_i, y_i) that would be fit.	37
5.6	A figure showing a plot of the pandel function over 300 nanoseconds with 10 meters, 30 meters and 50 meters of travel for the emitted light. The fit parameters, including λ_a and λ_s , are fit according to the IceCube parameters as described in [52].	41
5.7	A figure showing a plot of the CPandel function over -50 ns to 300 ns at 50 meters of travel distances for the emitted light. The parameters aside from σ are fit according to the simulated data, and we have two plots of $\sigma \in \{5 \text{ ns}, 10 \text{ ns}\}$.	43
5.8	Normalzied residual time distribution made using simulated events. Here the residual time is computed by comparing the geometric time with the true travel time simulated by the photon propogation software. This does not contain any dark noise or electronic noise and hence is an idealized distribution.	45
5.9	Distances from 0 to 30 meters.	46
5.10	Distance from 20 to 50 meters.	46
5.11	Distances from 40 to 70 meters.	46

5.12	Distances from 60 to 90 meters.	46
5.13	A snippet of data stacked over multiple channels using a POCAM flash as a source of light. The POCAM provides a 10 ns flash of light, and sits at a fixed distance from the Optical Module. The time has been shifted for convenience.	47
5.14	Linear interpolation of the STRAW data. This produces a likelihood distribution that has piecewise behaviours due to the linear nature.	48
5.15	Cubic interpolation of the STRAW data. The cubic fit allows for a smoother fit between points, but still has a piecewise nature due to the interpolation.	48
5.16	A data filtering method to help remove the background noise that is present in the STRAW data.	49
5.17	Varying exponential normal/gaussian distributions compared to the STRAW data.	50
6.1	A distribution of the solid angles for reconstructed and true directions using the linefit method. The solid angle is given in degrees for clarity.	55
6.2	A distribution of the solid angles for reconstructed and true directions using the likelihood method. The linefit reconstruction angular resolution is also plotted alongside a distribution for the likelihood given the true track as a starting point.	56

6.3 A distribution of the solid angles for reconstructed and true directions using the likelihood method seperated into zenith and azimuth components in degrees. Above: The zenith component distribution where $\Delta\theta = \theta_{\text{true}} - \theta_{\text{reco}}$ in the reconstruction process. Below: The azimuth component distribution where $\Delta\phi = \phi_{\text{true}} - \phi_{\text{reco}}$ in the reconstruction process.	57
6.4 Similar to the distribution in figure 6.2, the angular resolution is plotted in degrees into a histogram. Here the initial starting conditions are grouped into the true vertex, true direction and only linefit, where the former are given linefit parameters for the remaining parameters.	60
6.5 A distribution of the vertex zenith and azimuthal components when projected onto a sphere of radius 550 meters. Above: The zenith component distribution. Below: The azimuth component distribution.	62
6.6 A distribution of the vertex zenith and azimuthal components when projected onto a sphere of radius 550 meters. Above: The zenith component distribution. Below: The azimuth component distribution.	63
6.7 We plot the likelihood ratio ℓ_f/ℓ_i against the final reconstructed angular resolution using a heatmap.	64
6.8 Correlation heatmap between the initial negative loglikelihood value and the final negative loglikelihood.	65
6.9 Correlation map of the final reconstructed angular resolution and the initial angular resolution.	65

6.10 Distribution of the computation time for reconstructing events normalized by the pulse count. Higher energy events will naturally need to a larger number of observed pulses and increase the computation time accordingly	66
---	----

Chapter 1

Introduction

The cosmic sky has entranced humans for as far as recorded history can trace. As technology evolved, so too did the observation of the universe around us; from the naked eye to primitive telescopes, and eventually to present day space telescopes, like the Hubble Space Telescope and the upcoming James Web Space Telescope (**NEED TO CITE THESE**). These growing technological leaps have also resulted in the exploration of the incredibly small and eventually resulted in the discovery of the neutrino [50]. It was perhaps inevitable that these two seemingly separate areas of physics would eventually meet.

Will need to make this a general introduction to the topics, and less like the background.

Chapter 2

Background

2.1 Neutrinos

The neutrino is a fundamental particle first proposed by Wolfgang Pauli [17], and then later discovered in 1956 using the byproducts of β^- decay [50] in the form of the electron neutrino. As research continued into the elusive neutrino, another flavour of neutrino was discovered in 1962 called the muon neutrino (ν_μ) [22] and eventually the final flavour of the tau neutrino (ν_τ) [37].

2.1.1 Oscillations

Alongside the discovery of the neutrino and their flavours, another problem arose in the field of neutrino physics: the solar neutrino problem [40]. During the 1960's, an experiment was proposed by John Bahcall and Ray Davis to measure the solar neutrino flux, referred to as the Homestake experiment [23, 10]. This tank was filled with cleaning fluid which used ^{37}Cl as the active agent in detection. It was built

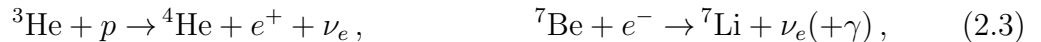
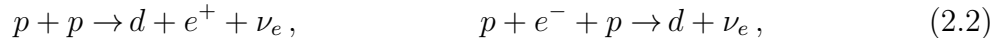
2.1. NEUTRINOS

underground to avoid cosmic backgrounds, and used the reaction[23, 10]

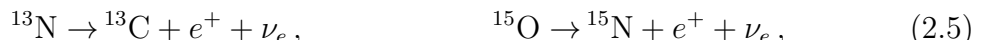


to measure the expected solar neutrino flux from the sun.

Solar neutrinos originate from nuclear processes that occur in the sun, mainly from the *pp* chain and the CNO cycle. The *pp* chain is described by the following reactions,



while the CNO cycle is described by



and can be detected in experiments on Earth [30, 29]. It is easy to see that through these processes the internal processes of the sun produce primarily electron neutrinos. Depending on the energy and process producing the neutrino, we can expect to detect this particular flavour of neutrino in experiments like the Homestake experiment. In particular, using the predicted distribution of the internal electron density of the Sun and a spectrum of the produced electron neutrinos, one could predict the expected flux of solar electron neutrinos [30]. Using these previous processes, one would expect

2.1. NEUTRINOS

the flux of solar neutrinos to be purely electron flavoured yet it was found that the measured flux of neutrinos was consistently around 30% the theoretical amount [23, 10, 30], and hence was coined the solar neutrino problem.

Neutrino detectors continued to be constructed to research and understand these fundamental particles, such as Kamiokande-II [32, 33] and Super-Kamiokande [59] from the collaboration of Kamiokande [32] and the IMB [18] experiments. The Kamiokande-II detector was a water cherenkov experiment for detecting ${}^8\text{B}$ solar neutrinos through the neutrino–electron scattering interaction

$$\nu_e + e^- \rightarrow \nu_e + e^- , \quad (2.7)$$

which yields information on the neutrino arrival time, the direction, and the energy spectrum [33]. This detector boasted 2140 tonnes of water viewed by an array of 20 inch diameter photomultiplier tubes. Collecting data for 450 days from January 1987, the experiment found results consistent with the Homestake ${}^{37}\text{Cl}$ experiment. The IMB experiment had a similar setup with a 3.3-kiloton fiducial mass and 2084 eight inch photomultiplier tubes, but was used to observe atmospheric neutrinos (neutrinos produced from cosmic ray interactions in the atmosphere) [18]. Yet again, the experiment found that the observed rates were lower than the theoretical expected rates [18]. To improve on these results and confirm they weren't statistical anomalies, the Super-Kamiokande detector was built as a 50-kiloton detector with 11,146 50–cm diameter photomultiplier tubes [32]. This massive upgrade from Kamiokande-II meant reduced uncertainties, and after detecting 900 muon-like and 983 electron-like events, the ratio of muon to electron neutrinos was compared to the expected theoretical result which again showed a reduced flux from expected [32]. The fact that these

2.1. NEUTRINOS

missing neutrinos were consistent between atmospheric and solar neutrinos meant there was something deeper going on than initially thought.

Another class of solar neutrino detectors were those that used the Gallium chain



such as GALLEX [57]. Regardless, the same issue persisted as there continued to be a distinct dissonance between the theoretical expectations of solar neutrinos and the observed experimental results. That was, until the Sudbury Neutrino Observatory (SNO) made a distinct change in their approach to solar neutrino detection compared to predecessors by using heavy water [11]. This allowed for the following interactions [11],



where we have the Charged Current (CC) interaction in equation 2.9, the Neutral Current (NC) interaction in equation 2.10 and the electron scattering interaction just like in equation 2.7. This meant that all flavours of neutrinos could be detected, and using it to detect solar neutrinos showed the theoretical flux originally predicted [11].

This result had an astounding implication; the neutrinos were changing on their journey from the Sun [11]. In the Standard Model, all the neutrino flavours have masses that are identically zero, and this would mean that there is no possible way for the neutrinos to somehow change flavour on their journey to the detectors [30]. Clearly there was a change in flavour, and thus the Standard Model must be incorrect

2.1. NEUTRINOS

about the masses of the neutrinos.

The classic demonstrative method to describe this is to consider the mixing of two neutrino flavours (like ν_μ and ν_e) [30]. In analogy to quark flavour mixing [24], we know the mixing of the flavours occurs in the transformation from the mass to the flavour basis. This means that the translation between considering the mass of the traveling neutrino against the flavour is non-trivial, and generally changing between one to the other is a super-position of states. In particular, for two mass and flavour states one can find [30],

$$P(\nu_e \rightarrow \nu_\mu, ct) = \sin^2 2\theta \sin^2 \left(\frac{\pi c t}{L} \right) \quad (2.11)$$

where θ is the mixing between the two flavour states, $L = \frac{4\pi E}{\Delta m^2}$ is the vacuum oscillation length, and $\Delta m^2 = m_2^2 - m_1^2$ is the difference between the two mass squared values. It is important to note that when we say Δm^2 , these mass values are not the masses of the flavour states, but rather values associated with another basis in which neutrinos travel [24]. Here it is easy enough to see that the oscillation probability vanishes if the masses are identical, and this naturally extends into the three flavour case. The vacuum oscillation length, L , is an important and useful quantity as it describes the distance a neutrino must travel before an oscillation is expected [30]; this behaves like the period of oscillation as it amplifies the probability of mixing for particular distances. Experiments like the long–baseline neutrino oscillation experiment Tokai–to–Kamioka (T2K) attempt to use this length to probe the mixing angles of the three neutrino flavours.

2.1. NEUTRINOS

Similar to the CKM matrix for quark mixing [24], the Pontecorvo–Maki–Nakagawa–Sakata (PMNS) matrix [43] gives a relation between the mass and flavour states:

$$\begin{bmatrix} \nu_e \\ \nu_\mu \\ \nu_\tau \end{bmatrix} = U \begin{bmatrix} \nu_1 \\ \nu_2 \\ \nu_3 \end{bmatrix} \quad (2.12)$$

and we see that

$$U = \begin{bmatrix} c_{12}c_{13} & s_{12}c_{13} & s_{13}e^{-i\delta_{\text{CP}}} \\ -s_{12}c_{23} - c_{12}s_{23}s_{13}e^{i\delta_{\text{CP}}} & c_{12}c_{23} - s_{12}s_{23}s_{13}e^{i\delta_{\text{CP}}} & s_{23}c_{13} \\ s_{12}s_{23} - c_{12}c_{23}s_{13}e^{i\delta_{\text{CP}}} & -c_{12}s_{23} - s_{12}c_{23}s_{13}e^{i\delta_{\text{CP}}} & c_{23}c_{13} \end{bmatrix} \begin{bmatrix} e^{i\eta_1} & 0 & 0 \\ 0 & e^{i\eta_2} & 0 \\ 0 & 0 & 1 \end{bmatrix} \quad (2.13)$$

where $s_{ij} = \sin \theta_{ij}$, $c_{ij} = \cos \theta_{ij}$, δ_{CP} is the Charge–Parity violation phase [43], and η_i are the Majorana phases. If neutrinos are not their own anti-particles, or in other words are Dirac fermions, we can expect $\eta_i = 0$. If they are their own anti-particles, also knowns as Majorana, then the phases η_i play a more imporant role [29].

2.1.2 Interactions

Neutrinos are neutral and interact only through the Weak interaction. The Weak interaction is a force that is mediated by the W^\pm and Z^0 massive bosons, and is the force responsible for decays. The main vertices involved in neutrino interactions are shown in Figure 2.1, where the interacting lepton corresponds with the interacting neutrino flavour.

All interaction involving neutrino production or detection utilize these vertices in some shape or form. We refer to interactions that use the W^\pm boson as the Charged

2.1. NEUTRINOS

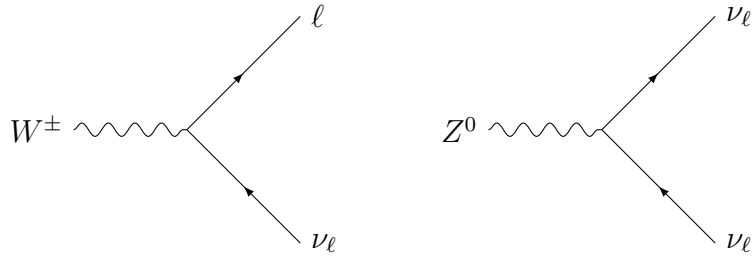


Figure 2.1: The Feynmann diagrams for the vertices that would be included in neutrino interactions using the charged W^\pm boson on the left and the neutral Z^0 boson on the right.

Current (CC) interaction [28], and those that use the Z^0 boson as being Neutral Current (NC) interactions [28].

It is natural to notice that these interactions require something to interact with, or in other words, the neutrinos must propagate through non-vacuum media and hit targets. We have up to this point only considered oscillations of neutrinos in vacuum, and another important aspect is to consider the effect interactions could have on these oscillations. In particular, it is noted that certain flavours of neutrinos can be more strongly influenced by media than others [30, 46]. Electrons are much more prevalent in matter than the other two generations (μ, τ) and hence the electron neutrino (ν_e) tends to experience a larger interaction than the other flavours [30, 46]. This difference in coupling results in changes in the oscillation that is complex.

This phenomena comes to a head with the Mikheyev–Smirnov–Wolfenstein (MSW) effect. The mixing angle and oscillation length vary with the electron density in the medium which varies the rate at which these neutrinos mix [30, 46]. In particular there is a resonance mixing angle (and hence resonance electron density) at which the mixing is maximized [30, 46]. The electron density at the centre of the sun starts

2.1. NEUTRINOS

far above the resonance and ends below the resonance at the edge, hence the produced electron neutrinos experience this resonance oscillation along their path out of the solar center [30, 46]. Neutrino oscillations are the reason for the solar neutrino problem, and the MSW effect is the catalyst [30].

2.1.3 Solar Production

As was discussed in subsection 2.1.1 and 2.1.2, neutrinos produced in the fusion process hold great historical significance, and in the attempt to resolve the solar neutrino problem we have come to better understand neutrinos and their processes. The leading reaction chain is the *pp* chain [29, 30], which is given by [29]

$$p + p \rightarrow d + e^+ + \nu_e . \quad (2.14)$$

All other chains that fall under the *pp* chain follow a similar idea; through the charged current interaction, there is the production of an electron neutrino during the fusion of two reactants [29].

2.1.4 Atmospheric Production

Another site where we can observe neutrino production is in the atmosphere [26, 29, 58]. These neutrinos are primarily produced by the decay of pions and muons [29],

$$\pi^+ \rightarrow \mu^+ + \nu_\mu , \quad (2.15)$$

$$\mu^+ \rightarrow e^+ + \nu_e + \bar{\nu}_\mu \quad (2.16)$$

2.1. NEUTRINOS

and the charge conjugate π^- [29]. The production of these decaying pions and muons is initiated by cosmic rays interacting with the nucleons in the atmosphere [26, 29, 58]. Looking at the inciting interactions, a natural and useful ratio is

$$\frac{\nu_\mu + \bar{\nu}_\mu}{\nu_e + \bar{\nu}_e} \quad (2.17)$$

of the number densities [29]. It is also useful to note that atmospheric neutrinos can be both downward heading and upward heading, as they can travel through the earth. These two different directions will experience different travel lengths and can be used to probe neutrino oscillations [29]. There have been studies done on the atmospheric neutrino flux with experiments across the globe [29, 58].

2.1.5 Geological Production

Neutrinos can also be generated by the natural decay of rare elements in the Earth's crust [12]. In particular, the main source is of β^- decays in elements like ^{238}U , ^{232}Th and ^{40}K [12]. Measuring the geo-neutrino flux holds interesting consequences in the geology and physics community, for example predictions of the radiogenic contributions by neutrino producing processes can be predicted [12].

2.1.6 Reactor Production

Production of neutrinos by β^- decay also occurs in reactors [49]. The fission process involving ^{235}U uses a chain reaction of neutron production to fuel more fissions [49], and this neutron rich environment promotes the classic bound neutron decay,

$$n \rightarrow p + e^- + \bar{\nu}_e . \quad (2.18)$$

2.1. NEUTRINOS

The benefit of using reactor neutrinos lies in the flavour purity; the production mechanism promotes the creation of electron anti-neutrinos [49].

2.1.7 Accelerator Production

Accelerator neutrinos are produced by firing a beam of protons at a target to produce secondary mesons that decay and produce neutrinos [38]. This process is similar to the atmospheric neutrino production process as the idea is similar: secondary mesons produced by high energy primaries that then decay and produce neutrinos. The benefit of this production method is they are generally produced in a collimated beam within some angular range due to the momentum based production [38]. This effectively produces a neutrino beam that can then be used in later processing.

2.1.8 Galactic Production

Supernovas can produce high energy neutrinos that can travel thousands of years before reaching detectors on earth [42]. These provide both unique insights into the universe, as they will leave a higher energy signature [42] and the vast distance travelled allows for the neutrino to arrive at the earth in a mass eigenstate. The reason for arriving in the eigenstate occurs as a result of the large distance allowing for the competing mass states to decouple [42].

Another proposed galactic source of high energy neutrinos are Active Galactic Nuclei (AGN) which are potentially the most powerful producers of radiation in the universe [16]. AGNs are known for accelerating protons up to $10^{20} - 10^{21}$ eV, and provide a potential pathway for producing incredibly high energy neutrinos [16].

2.2. DETECTION TECHNIQUES

2.2 Detection Techniques

With a plethora of neutrino sources, some of which have been discussed, the method of detection becomes increasingly important. For the purposes of this text, we only consider a couple of techniques that are of interest. To begin, we can consider the GALLAX type experiments that use the chain identified in equation 2.8.

2.2.1 Germanium Detectors

These are blind to the other flavours of neutrinos, as was already discussed, but they did motivate using Germanium as a potential neutrino detection method. In particular there are propositions that these detectors may provide $\mathcal{O}(1\text{kg})$ mass, $\mathcal{O}(100\text{eV})$ threshold and $\mathcal{O}(1\text{kg}^{-1}\text{keV}^{-1}\text{day}^{-1})$ background experiments [53]. In particular, detectors like these could be sensitive to low energy solar neutrinos through neutrino–nucleus elastic scattering [14] where the lower energy neutrinos can have an amplified signal through internal charge amplification [14].

2.2.2 Calorimeters

Another class of neutrino detectors use calorimeters as a method of detecting energy deposits from secondaries in neutrino producing processes [25, 39]. These signals can then be used to reconstruct the neutrino flavour and energies [25, 39]. Two examples of such detectors are MINOS [25] and ICAL [39]. The former uses a proton beam on a graphite target to produce showers of hadrons that are then focused by two magnetic horns in a calorimeter [25]. These hadron showers consist of pions and, at higher energies, kaons which produce our neutrinos in their decays [25]. ICAL is a calorimeter array located at the India–based Neutrino Observatory [39] that can

2.2. DETECTION TECHNIQUES

use external sources of neutrinos (atmospheric) to probe the mixing angles [39]. In particular ICAL can be particularly sensitive between neutrinos and anti-neutrinos [39].

2.2.3 Vavilov–Cherenkov

Now that we have an appreciation for some novel techniques in detecting neutrinos, we discuss one that is of particular interest for the purposes of this thesis: Vavilov–Cherenkov (VC) Radiation. VC Radiation was discovered in 1934 by Vavilov [56] and Cherenkov [19] and then later in 1937 explained by Tamm and Frank [54]. In essence, VC Radiation is the emission of electromagnetic radiation due to a charged particle traveling in a medium at a velocity, v , that exceeds the phase velocity, v_p , of light in that medium [27]. In particular, if we suppose the velocity of light in vacuum is c , then VC Radiation will occur if

$$v > v_p = \frac{c}{n(\omega)}, \quad (2.19)$$

where $n(\omega)$ is the frequency dependent index of refraction in that medium [27]. In particular, if the light is emitted along a wave–vector \vec{k} from a charged particle traveling with velocity \vec{v} , then the angle between the two vectors is θ_0 and can be described by

$$\cos \theta_0 = \frac{c}{n(\omega) \cdot v} \quad (2.20)$$

where $v = |\vec{v}|$ [27]. Due to the electromagnetic radiation wavefront being a result of spherical emissions [27], the process is very similar to that of the acoustic sonic boom for macroscopic objects [27] which serves as an excellent analogy.

2.3. NEUTRINO TELESCOPES

This particular form of radiation is incredibly useful for neutrino detection. We can use the secondary leptons produced in CC interactions, like those in Figure 2.1, to produce VC Radiation that can be detected by ultra sensitive photon detectors.

2.3 Neutrino Telescopes

Generally one considers only telescopes as those that utilise the visible part of the electromagnetic spectrum, and in general this is true, but as technology has advanced we have found that using even other wavelengths of light has resulted in different information to be gained from the imaging of the universe. This idea can be extended to include other sources or even particles to image with, like the neutrino. Due to the weakly interacting nature of the neutrino it can travel great distances before interacting and can provide direct sources where cosmic rays may be ambiguous about their source. Neutrino telescopes use exactly this principle to reconstruct neutrinos from cosmic sources with the potential to image the sky one day in an entirely different lens.

The DUMAND experiment [9] was the first to propose the use of large photomultiplier tubes in deep ocean to detect high energy neutrinos. Though it was never brought to fruition, it was the first of its kind and paved the way for future VC Radiation based neutrino telescopes such as Baikal [13], AMANDA [8], ANTARES [6], and IceCube [4]. We will discuss a few of these that are relevant.

2.3.1 IceCube

The IceCube Neutrino Observatory is a cubic-kilometer neutrino detector built in the Antarctic ice [4]. Its primary scientific goal was the detection and characterization of

2.3. NEUTRINO TELESCOPES

astrophysical neutrinos along with their sources [4], but also has many other scientific goals including indirect detection of dark matter, exotic particle searches, neutrino oscillations, and supernova neutrinos [4].

Neutrino detection occurs through V_C Radiation of charged particles from neutrino interactions traveling through the ice [4]. IceCube has the advantage of having a very large volume coverage in order to compensate for the small neutrino cross-section and low astrophysical sources flux [4]. The detection is done through the Digital Optical Module (DOM) consisting of 10'' Photo-Multiplier Tubes (PMTs) which are sensitive to the V_C photons [4]. The full array is has 5160 DOMs on 86 vertical strings where each string consists of 60 DOMs [4]. The array sits between 1450 meters and 2450 meters below the surface of the ice [4].

The detection medium of ice is novel in the neutrino telescope field and offers both advantages and disadvantages over water [36]. Ice that has been undisturbed, like that in the Antarctic, offers pure conditions and is stationary when compared with the flow of most large bodies of water [36]. However, equipment that is used in the ice is not recoverable [36] and hence difficult to repair. Moreover, ice offers a shorter scattering length than one would expect in water [36] and due to the ice being layered this effect is layer dependent and was studied in detail to build reference tables [36].

IceCube has been successful in its original physics goal [4] and in 2017 detected a high energy neutrino estimated to have an energy of 290 TeV [3]. This was coincident in direction and time with a gamma-ray flare from blazar TXS 0506+056 [3]. Studying previously collected data in search for more high energy events of the same caliber from the same direction supported the claim that blazars can be a source of high energy neutrinos [3]. IceCube is continuing to collect data and explore more of

2.3. NEUTRINO TELESCOPES

its physics goals.

2.3.2 ANTARES

The ANTARES neutrino telescope is the first operational neutrino telescope in the Mediterranean Sea [6] adopting heavily from DUMAND [9] and Baikal [13]. Similar to other neutrino telescopes, the main method of neutrino detection arises from VC Radiation from secondary leptons produced in neutrino interactions [6]. The array is composed of 12 mooring lines equipped with 25 Optical Modules (OMs) that contain PMTs for a total of 885 OMs (the 12th line has a different number of OMs) [6].

Compared to the experiments that use ice, like Icecube [4, 3, 36] and AMANDA [8], ANTARES uses ocean water as the medium of VC Radiation from high energy neutrino induced leptons [6]. The benefit over ice is that the attenuation/scattering length is longer, and the lack of layering reduces the reconstruction difficulties [6, 36]. The difficulties are that the water shifts, and hence can both rotate the detectors slightly and move their relative positions [6, 36]. To account for this shifting, ANTARES uses a High Frequency Long Base Line (HFLBL) acoustic system providing 3D positions of hydrophones positioned along the mooring lines [6]. To account for the tilting, each OM is given a set of tiltmeter–compass sensors giving the local tilt angles of each OM structure [6]. Moreover, there are backgrounds from ^{40}K decay and bioluminescence to consider [36].

ANTARES was finished construction in 2008 and has been collecting data since [6]. They have achieved their design goals and are able to achieve a positional accuracy better than 20 cm for each OM with the expected time resolution of 1 ns [6]. This experiment shows the feasibility of water based neutrino telescopes and opens the

2.3. NEUTRINO TELESCOPES

doors for future ocean neutrino telescopes.

2.3.3 KM3NET

Chapter 3

The Pacific Ocean Neutrino Explorer

The Pacific Ocean Neutrino Explorer (P–ONE) is a proposed neutrino telescope planned to operate in the Pacific Ocean near the West Coast of Vancouver Island, Canada [7]. As with other neutrino telescopes, P–ONE aims to detect and characterize extremely high energy astrophysical neutrinos from galactic and extra–galactic sources [7]. In particular, due to the planned multi–cubic kilometer coverage, it would be suitable for neutrinos from sources such as Blazars [3]. Moreover P–ONE hopes to provide an avenue for research in exotic particle searches, dark matter, neutrino oscillations, supernova neutrinos, and tau neutrino studies (ν_τ) [7].

3.1 Geometry

The geometry of the detector is incredibly important, as the layout and positions of the detectors can drastically change the results and the sensitivities [4]. The first proposed Explorer phase for P–ONE corresponds to the first 10 string–segment to be deployed [7]. Each string will be composed of 20 photo–sensors and at least two calibration modules [7], with the strings organized in an array similar to that of IceCube [7, 4]. In order to avoid using thousands of strings to get a larger coverage,

3.2. DETECTORS

it can achieve a similar amount of information using a segmented approach where six more arrays similar to those of the Explorer are added around it [7]. This design is drawn in Figure 3.1.

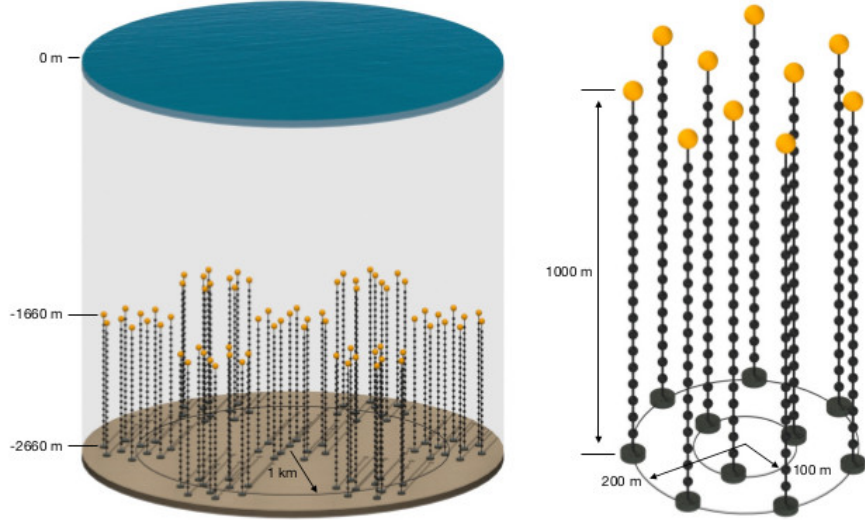


Figure 3.1: Left: Proposed full detector of the P-ONE detector. Right: Proposed array for the Explorer deployment of P-ONE.

With the current proposed geometry, the detector will be incredibly sensitive to horizontal incoming high energy muons from astrophysical neutrino sources [7].

3.2 Detectors

Similar to previously constructed neutrino telescopes, P-ONE will primarily use Vavilov–Cherenkov Radiation from leptons produced through neutrino interactions. This electromagnetic radiation is then detected through highly sensitive optical modules containing photomultiplier tubes (PMTs).

3.2. DETECTORS

3.2.1 Photomultiplier Tubes

A key part of any neutrino telescope is the detection mechanism, and in this community the PMT is synonymous with detector. The PMT is a vacuum-sealed photocathode with dynode and anodes above connector pins [31]. The primary mechanism of a PMT is the photoelectric effect from a photon hitting the photocathode [41]. This ejected electron then travels and collides with another cathode, which results in more electrons being ejected. This results in a cascade of electron showers along the dynodes and anodes amplifying the signal before it reaches the connector pins [41]. Through this method the PMT can produce large signals at the single photon level, yet is only sensitive to a particular range of frequencies/wavelengths of light for the same reason [41].

In particular, PMTs are generally sensitive to wavelengths anywhere as low as 100 nm to as high as 500 nm depending on the material of the photocathode [31]. Another property of PMTs to note is the Quantum Efficiency (QE), which is defined as the ratio of photoelectrons emitted by the photocathode to the number of incident photons [31]. Thus, QE defines the probability an incident photon causes a signal. The QE is dependent upon the photocathode and varies with the incident photons wavelength, as different wavelengths carry different energies [31].

In contrast to QE, the Dark Current (Dark Noise) is the reporting by PMTs of light even in completely dark environments [31]. According to the Hamamatsu handbook [31], a number of reasons can be the cause for this misfiring in PMTs including (but not limited to) thermionic emissions, internal current leakage, scintillation from glass envelope and radiation sources. One can minimize the effect from these sources, such as reducing the temperature to limit the thermionic emissions [31].

3.2. DETECTORS

The final aspect of PMTs we discuss is afterpulsing, the small pulses observed after the arrival of a signal [31]. The quick afterpulses (within nano–seconds) can usually be attributed to scattering of electrons on the first dynode [31], while later afterpulses (within microseconds) can be the result of positive ions from the ionization of residual gases in the tube [31].

The PMT is an incredibly technical piece of hardware, and characterizing each PMT is important to understanding the detector as a whole.

3.2.2 Digital Optical Modules

In IceCube, the Digital Optical Module (DOM) is a module containing a ten-inch PMT supported by coupling gel, the high voltage generator, an LED flasher board for calibration, and the mainboard used for analog and digital signal processing [5, 4] which allows for near-autonomous function. P–ONE will be adopting this approach for detector construction.

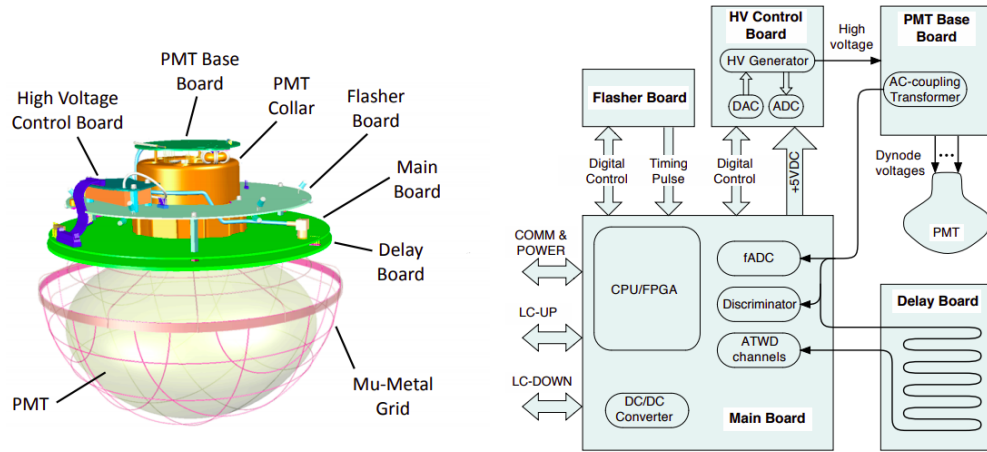


Figure 3.2: A diagram and schematic of the IceCube DOM.

Figure 3.2 shows a diagram of the IceCube DOM along with a schematic of the

3.3. STRINGS FOR ABSORPTION LENGTH IN WATER

electronics that are on board.

3.2.3 mDOMs

A proposed redesign of the IceCube DOM to increase the granularity of light detection is the multi-DOM (mDOM). In place of one large PMT, multiple smaller PMTs can line the same space and provide coverage at the cost of gaps between detectors. The benefit being that individual hits on the smaller PMTs can provide extra information using the acceptance angle and directionality of that particular PMT [20]. Moreover, in theory this can also reproduce the standard DOM data as the signal collected by a single PMT in the array can be collected and treated as a hit for the entire DOM. This gives the mDOMs a flexibility that isn't present for standard DOMs. In IceCube the standard DOMs use a ten-inch diameter PMTs [4], where the mDOMs would use up to 24 three-inch diameter PMTs [20]. Another point to note is that the photocathode area plays an important role in the amount of photons that can be detected, and hence the amount of information that can be collected from an event [4].

3.3 Strings for Absorption length in Water

The pioneer (sometimes referred to as pathfinder) mission for P-ONE is the STRings for Absroption length in Water (STRAW) and its follow up STRAW-b, which were deployed in 2018 and 2020 respectively. The purpose of these missions was to test the technical details of running an experiment like P-ONE, in particular the hardware limitation, to provide data to measure the attenuation length of light in water for light in wavelengths between 350 nm and 600 nm, characterize the bioluminescence

3.3. STRINGS FOR ABSORPTION LENGTH IN WATER

of deep-sea living organisms and the ^{40}K dissolved in the salty water [15].

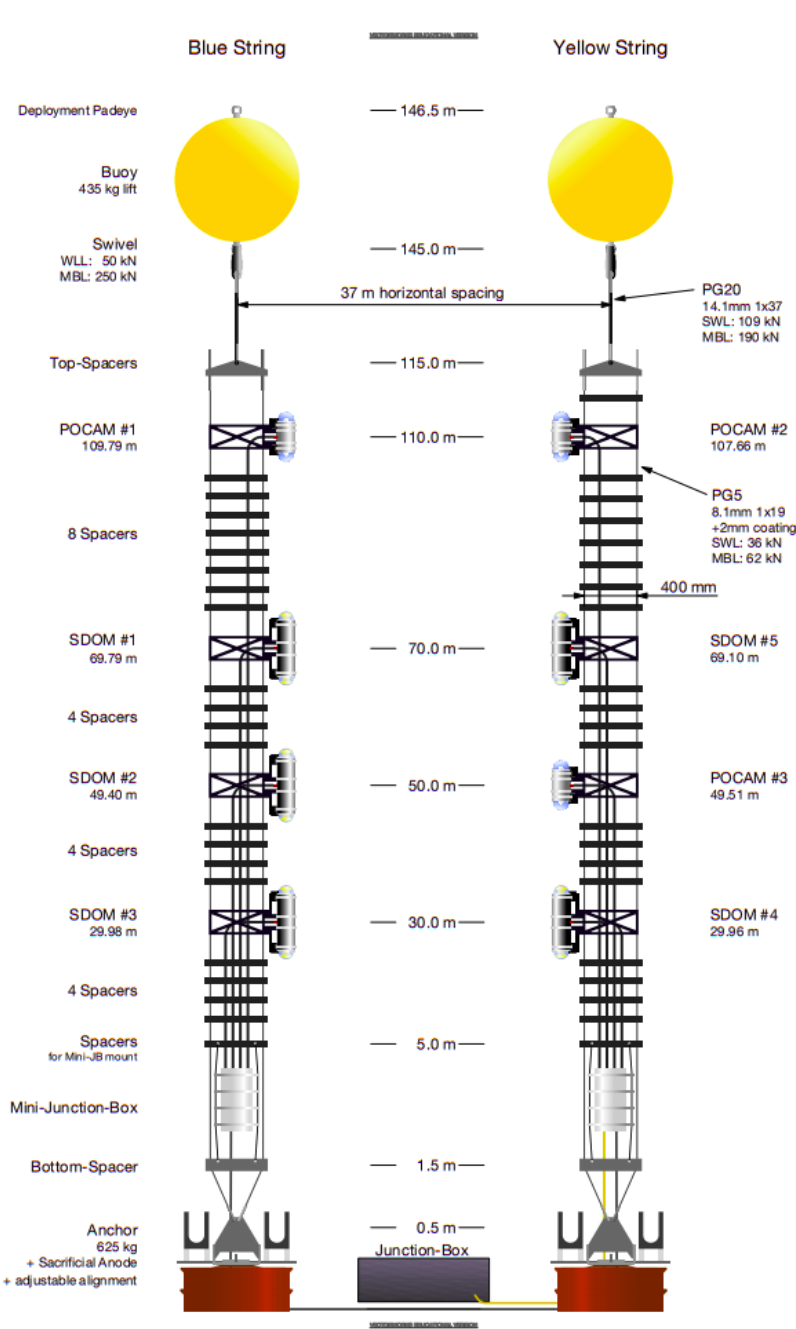


Figure 3.3: A diagram of the full STRAW setup including distances [15].

3.4. OCEAN NETWORKS CANADA

The basic design of STRAW, as shown in Figure 3.3, is the same as that of standard neutrino telescopes; using PMTs for detecting photons and calibrating light emitting sources on mooring lines to collect data [15]. In this particular case STRAW uses two vertical mooring lines with 3" PMTs and Precision Optical Calibration Modules (POCAMS) for the calibration sources [15], which provide isotropic and short pulsed flashes of light. The POCAMS are the powerhouse of this endeavour. They offer an adjustable source of intense isotropic light ($\mathcal{O}(10^9)$) [34]. The glass hemispheres that house the POCAMS provide a transmissivity of $> 95\%$ in the range between 350nm and 600nm [34]. The attenuation length L_T in water can be determined using the known photon intensity N_0 , the wavelength from the POCAM flashes and the distance r to each particular PMT with effective collection area A_{det} measuring an intensity $N(r)$ [15]. This yields

$$N(r) = \frac{N_0}{4\pi r^2} \exp\left(-\frac{r}{L_T}\right) A_{\text{det}}. \quad (3.1)$$

The expected maximum value of absorption length is around 50 meters, so the STRAW geometry has been chosen to cover the ranges between 20 m and 90 m [15]. Some of the geometry choices were purely due to technical limitations, such as the maximum safe cable lengths to minimize data loss [15], while others were to preserve some form of symmetry between modules [15].

3.4 Ocean Networks Canada

The construction and implementation of P-ONE is supported by Ocean Networks Canada (ONC), an oceanography observatory with a vast network monitoring the west and east coasts of Canada along with the arctic [2]. Situated at the University

3.4. OCEAN NETWORKS CANADA

of Victoria, ONC uses cabled observatories, remote control systems and interactive sensors for data collection and evidence-based decision-making [2].



Figure 3.4: A diagram of the Ocean Networks Canada Western Infrastructure for monitoring the Pacific Ocean. This contains the NEPTUNE and VENUS observatories. Source [2].

The west coast observatory, shown in Figure 3.4, is comprised of the 800-km NEPTUNE observatory and the nearly 50-km VENUS observatory [2], with the NEPTUNE observatory housing the proposed site of P-ONE at the Cascadia Basin. The Cascadia Basin, as seen in Figure 3.5, is a heavily sedimented abyssal plain located 2660 meters below sea level [2]. Though the environment seems inhospitable, with temperatures below 2°, high-pressure, and a distinct lack of light, one can still find organisms highly adapted to the extreme environment [2].

This biodiversity results in the potential background of bioluminescence [7, 2, 60, 45]. Bioluminescence is the emission of visible light by living organisms due to natural chemical processes used by a wide range of species [60]. Some studies show that

3.4. OCEAN NETWORKS CANADA

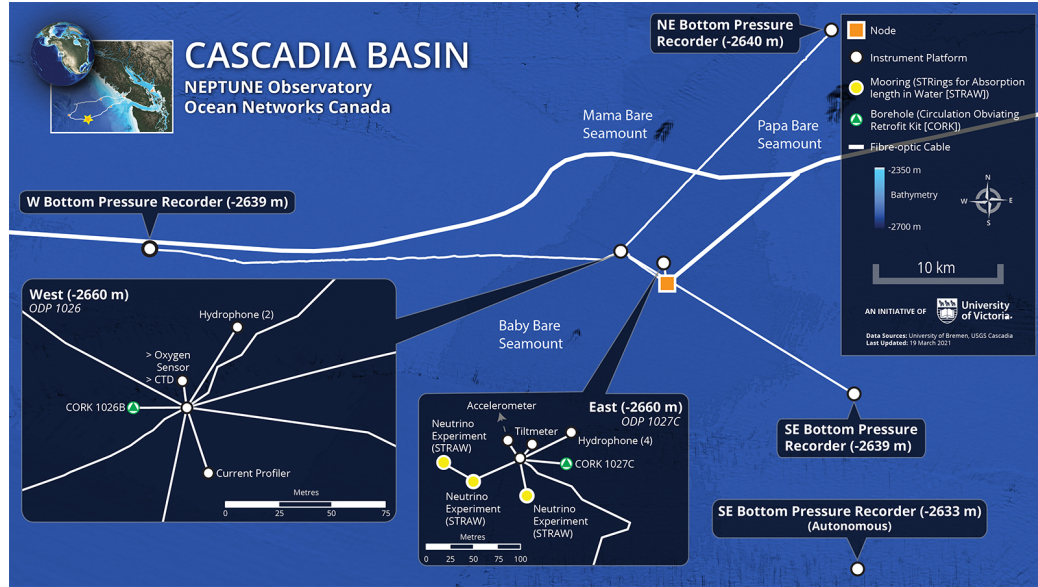


Figure 3.5: Diagram of the Cascadia Basin, the site of the upcoming P-ONE experiment and current site of the pathfinder STRAW. Source [2].

75% of all organisms larger than 1 cm occurring below the surface down to 4000 m depth are capable of bioluminescence [45]. Due to evolutionary advantages, most bioluminescent organisms emit light between 440 nm and 540 nm, which also has the largest absorption length in water [60]. The amount of photons emitted can also vary significantly from 10^3 for bacterium to 10^{12} photons from some fish [60]. There are efforts being put together to understand and characterize this background in order to be better prepared for when the detector is installed.

Chapter 4

Simulation

As P–ONE has only deployed the Pathfinder missions thus far, including STRAW and STRAWb, the data used in this thesis is primarily simulated. In particular, the data needs to be usable to test and build a reconstruction algorithim for muon–neutrinos. This means simulating muon tracks. For this reason, we lightly cover the simulation process used to produce data including the pre-existing IceCube Framework, Simulating Neutrinos, Simulating Muons and the Detector Response.

4.1 IceCube Framework

The software framework already exists from IceCube, and in order to minimize the amount of new code needed to simulate P–ONE it is simplest to use the IceCube software. In particular, the software documentation is readily available [1] and referred to as IceTray. This is meant to be a full framework capable of simulating, reconstructing and analysis all in one [1]. For the purposes of P–ONE, we wish to only use the simulation subset of the framework as it is primarily made using open-source software, and hence can avoid potential proprietary issues.

The bulk of the code is written in C++ with the goal of being modular. This means

4.2. SIMULATING NEUTRINOS

that rather than writing scripts that call functions or classes that are pre-existing, the code is designed so that there is a single steering script that calls modules to run tasks including the simulation of muons or neutrinos, and including geometry files. Modules can be added by users as well to then be included in the steering scripts. The code has also been wrapped using Python so that modules can be reached via python scripts, and hence steering scripts can be written in Python. For this reason, Python is the language of choice for the purposes of this work.

4.2 Simulating Neutrinos

The software used to generate neutrinos is the very aptly named Neutrino-Generator (NuGen) [1]. This is code written in IceTray based off of the All Neutrino Interaction Generator (ANIS), a high energy neutrino generator used for neutrino telescopes. NuGen has the capabilities of preparing and injecting a neutrino and interacting along the way if they so happen, and then forcing an interaction in the detector. NuGen can also produce secondaries. However, NuGen does not propagate photons nor charged leptons. This is saved for PROPOSAL and CLSim, where the former is used to propagate charged leptons and the latter is used to produce and propagate photons in a parallel manner (if using GPUs).

4.3 Simulating Muons

The module used to generate muons is the MuonGun that exists in GEANT4. This can be used to inject muons based on some sampling surface dependent upon a given flux model [1]. Muon Gun is versatile as it can be easily modified to produce muons using a variety of sampling surfaces, and can even be modified to be energy dependent

4.4. DETECTOR RESPONSE

[1].

In particular, the MuonGun works by drawing samples from a parameterization of the atmospheric muon flux [1]. This is parameterized in the same manner as described in [44]; it depends on the water depth (h), zenith angle (θ), multiplicity, and energy. In particular, the energy spectrum of single muons is described by

$$\frac{dN}{d(\log_{10} E_\mu)} = G \cdot E_\mu e^{\beta X(1-\gamma)} [E_\mu + \epsilon(1 - e^{-\beta X})]^{-\gamma}, \quad (4.1)$$

where there are multiple fit parameters described more in [44]. The energy loss due to water interactions also have to be added and are also discussed in [44]. These parameterizations are great for fast generation of muons [44], which is important for understanding the background of cosmic ray muons common in most neutrino telescopes [4, 6, 8, 7, 44].

Do we talk about Muon Gun or Cosmic Muons? Currently only Cosmic Muons are being used but both could be used.

4.4 Detector Response

The choice of geometry is incredibly important, as varying the position and number of detectors can, as one would expect, result in large changes in the performance of the detector (**WHERE TO CITE THIS FROM?**). The current proposed first stage of P-ONE is to be a pair of nested circles with the inner containing three strings and the outer containing 7 [7], as we can see in Figure 3.1. The simulated geometry is based off of this first design and held in a “.gcd” file which is used by IceTray [1]. **GET IMAGE OF GCD HERE SOMEHOW**. If we wish to see how the potential detector performance is affected by varying the geometry, we can change

4.4. DETECTOR RESPONSE

this geometry file and measure parameters such as the effective area to see how well it compares.

One of the most useful and widely used methods of measuring a neutrino detectors performance at a glance is the effective area. For a given particle of interest with some flux, the effective area is defined as the area of the detector scaled by the efficiency of the detector in measuring this particle [35]. Another way of phrasing this is that the effective area is that which detects perfectly the particles entering it for a given number of detections. Computing the effective area is non-trivial, as it is particle, flavour, energy, and direction dependent.

This has to include the detector geometry (GCD) files, the DOMs, and efficiency...?

Chapter 5

Reconstruction

A telescope is only as good as it's ability to identify distinct sources. In the case of a neutrino telescope this translates directly to how well observed events can be reconstructed for their direction. IceCube uses several reconstruction methods [4] and has several data quality checks required before a result is given any weight. Similarly, ANTARES has had years of work put into the reconstruction software in order to reach the accuracies it can now achieve [6]. To set the context for reconstructions, we need to first understand the data that is collected and how it is available.

5.1 Geometry of a Single Hit

At first thought, it may sound simple to try and reproduce the tracks that produce the light one would observe in neutrino detectors, but upon considering the data that is aquired the true complexity is revealed. To see this, consider first the geometry of a single hit to see what the data would look like. Referring to Figure 5.1 a muon track that is infinite in length is a safe approximation assuming a sufficient energy of the neutrino relative to the size of the detector. Specifically the track can be

5.1. GEOMETRY OF A SINGLE HIT

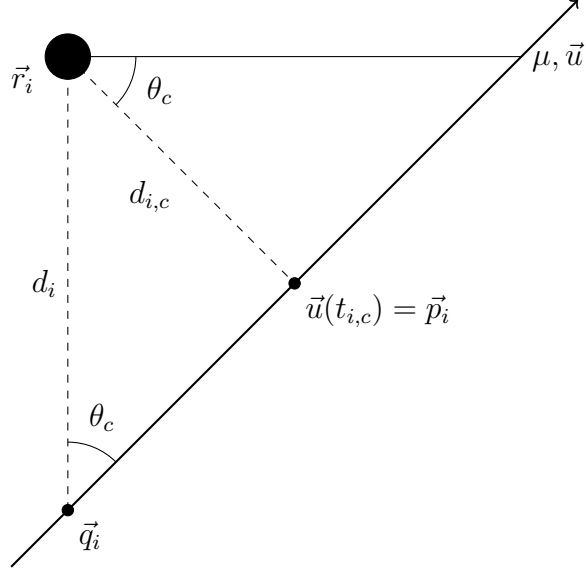


Figure 5.1: Drawing of muon track and Vavilov-Cherenkov Radiation hitting a single DOM where \vec{r}_i is the DOM location, \vec{q}_i is the emission point of the photon, and d_i is the distance the photon travels to the DOM.

parameterized with

$$\vec{u}(t) = \vec{x} + ct\vec{v}, \quad (5.1)$$

where \vec{x} is the vertex, \vec{v} is the direction in which the muon is travelling, t is the time parameter, and finally c is the speed of light, which for sufficiently high energy muons is a good approximation for the speed. Looking at the i^{th} DOM located at a position \vec{r}_i , it is easy to see there must be a closest approach position for the track, \vec{p}_i , and an emission point of a photon given there is a direct hit on the DOM, located at \vec{q}_i . The photon is emitted at a cherenkov angle of θ_c , which is as described in equation 2.20.

The next step is to consider the information known about the DOMs. In particular, the direction in which the DOM is facing will determine its angular acceptance giving information on whether or not particular photons can actually reach the DOMs, and the time at which photons are detected. Moreover, light can scatter and may

5.1. GEOMETRY OF A SINGLE HIT

not travel a direct path, so the distance d_i also becomes an important parameter to consider. Any sophisticated reconstruction technique will require these parameters to produce reliable results, and hence are important to both understand and compute given a track. Hence, the method for computing these parameters given a DOM position and track will be discussed.

Assuming a track as given in Equation 5.1, and that the closest approach position is at \vec{p}_i for a DOM at \vec{r}_i , then it can be easily computed that $d_{i,c} = |\vec{p}_i - \vec{r}_i|$. Using the closest approach distance,

$$d_i = \frac{d_{i,c}}{\sin \theta_c} \quad (5.2)$$

will describe the distance the photon travels. To get the emission point of the photon \vec{q}_i , it can be seen that $s_i = d_i / \tan \theta_c$ and that the corresponding time would be $t_s = s/c$. Then

$$\vec{q}_i = \vec{p}_i - ct_s \vec{v} = \vec{p}_i - s \vec{v}, \quad (5.3)$$

where $\vec{p}_i = \vec{u}(t_{i,c}) = \vec{x} + ct_{i,c} \vec{v}$. Due to the photon being emitted before the point of closest approach to the DOM, the distance (s) will be negative and thus

$$\vec{q}_i = \vec{x} + (ct_{i,c} - s) \vec{v}. \quad (5.4)$$

Now, the emission point and the distance d_i from equation 5.2 is known. Now, to compute the geometric time, as in the expected photon arrival time at the DOM from the proposed track. To predict this time, a reference along the track is needed, and the vertex \vec{x} is a natural choice for this. Then,

$$t_{\text{geo}} = t_d + t_x \quad (5.5)$$

5.1. GEOMETRY OF A SINGLE HIT

where

$$t_d = \frac{d_i}{c_n}, \quad \& \quad t_x = \frac{(\vec{q}_i - \vec{x}) \cdot \vec{v}}{c}. \quad (5.6)$$

In Equation 5.6 the former is the time it takes for the emitted photon to travel directly to the DOM, with c_n being the group velocity of light in water, and the latter is the time it takes for the muon to travel from the vertex to the emission point. It is important to note that in the second term of Equation 5.6, the numerator makes sure that the travel time has the correct value. Since the vertex \vec{x} is not physical, and is merely a reference point for the purposes of this thesis, it is possible for this location to be after the emission point. In that case, the value t_x would have to be negative, and this projection onto the direction vector of the track ensures this. Now, given the time at which the muon is at the vertex, the travel time can be augmented using a shifted t_{geo} that will now be comparable to the time that the DOM reports, t_{obs} . The parameter of importance then is the residual time, defined as

$$t_{\text{res}} = t_{\text{obs}} - t_{\text{geo}}, \quad (5.7)$$

as it will vaguely inform of the difference between the geometric guess track and the true track.

The next step is to recall all these prior computations rely on the distance of closest approach ($d_{i,c}$) being known. To compute this, geometric considerations with the vectors of the track, the DOM and the vertex need to be considered. To visualize the vector algebra, an origin is introduced from which the vectors can be drawn, in which case Figure 5.2 is obtained. The vector pointing to the vertex is \vec{x} and the vector pointing to the DOM is \vec{r} , where the indices are dropped for convenience.

5.1. GEOMETRY OF A SINGLE HIT

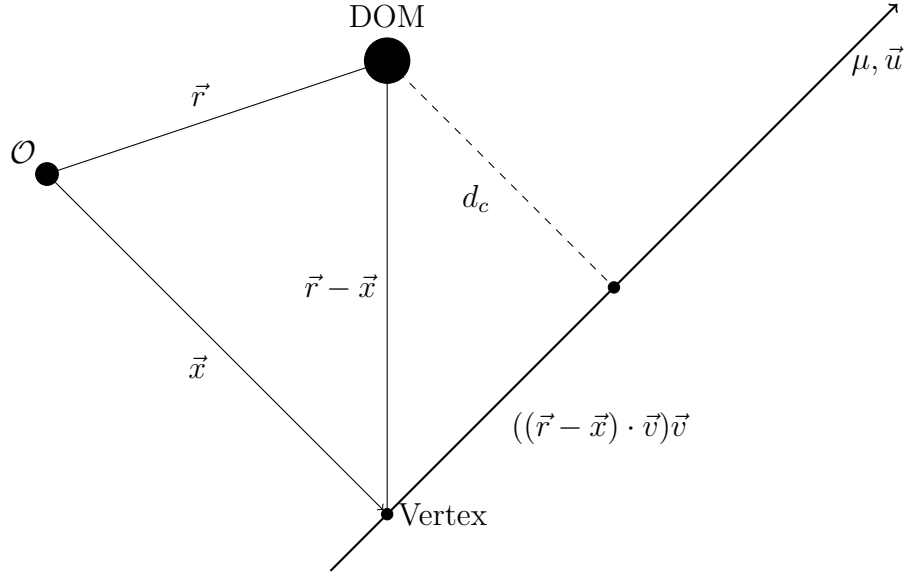


Figure 5.2: Drawing of a track with vertex and DOM labeled. The origin here is also marked to emphasize the vector notation and algebra. It is easy enough to see the vector algebra required to get the distance of closest approach through this diagram.

Then a vector pointing from the vertex to the DOM can be defined by $\vec{r} - \vec{x}$. Next, the projection of this vector along the track direction (which is already a unit vector) is $(\vec{r} - \vec{x}) \cdot \vec{v}$. Then, with two sides of a right angle triangle and the third missing side being the length d_c , so

$$d_c = \sqrt{|\vec{r} - \vec{x}|^2 - |(\vec{r} - \vec{x}) \cdot \vec{v}|^2}. \quad (5.8)$$

There is now a method of computing $d_{i,c}$, and thus computing d_i and t_{res} for each DOM given a proposed track $\vec{u}(t) = \vec{x} + ct\vec{v}$. It is important here to note the degrees of freedom that parameterizing a track have. The vertex provides four as it is a position in 3-dimensional space with a time. The direction provides two degrees of freedom, as it is a unit vector and can be parameterized using two angles and a unit

5.1. GEOMETRY OF A SINGLE HIT

length radius in spherical coordinates. This gives six parameters in total that need to be computed to uniquely define an infinite track.

A simple way to check that this is working is to plot the arrival times of photons on a single line of detectors whilst varying the direction of the track. Take these detectors to be located starting at the origin and located along the z-axis in space. If a track is traveling such that it intersects the central detector, the arrival times of the photons emitted by this track will take on a well defined shape. Figures 5.3 and 5.4 show these distributions given particular track directions with the zenith angle of direction provided. Of the directions given, there is also the special angle of $\theta = \pi/2 \pm \theta_c$ which lines up the wavefront with the line of detectors and hence has one of the “arms” of the arrival times be populated with coincident hits (they can be slightly off due to approximations).

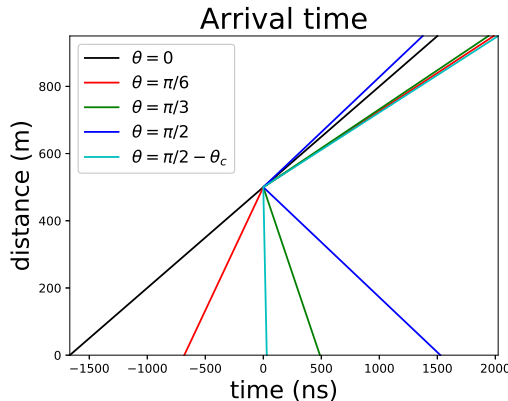


Figure 5.3: Upward Arrival Time

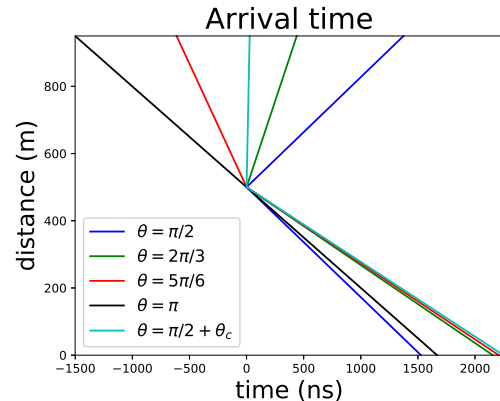


Figure 5.4: Downward Arrival Time

Now consider different methods for computing these parameters. There are several software techniques that need to be applied before a result can be taken seriously, and usually this pipeline begins with a simple and quick initial guess fit.

5.2. LINEFIT

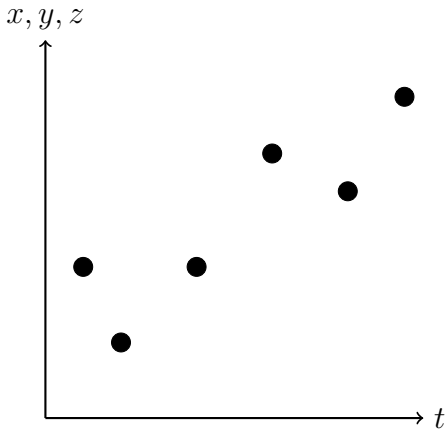


Figure 5.5: Drawing of the position and time space with possible points (x_i, y_i) that would be fit.

5.2 Linefit

Any robust reconstruction method requires an initial guess (generally referred to as a seed) in order to be used, but getting this first guess can be non-trivial. Moreover, reconstruction pipelines can be incredibly sensitive to the initial guess and ensuring the quality of this preliminary fit is difficult in its own right. The standard method for a first guess in such situations is the linear fit. This is a simple track fit that minimizes the χ^2 for the observed hits in an event. As such, this fitting technique assumes that all hits on the DOMs are directly on the path of the muon track, which is a reasonable first approximation.

Under these approximations, assume each spatial coordinate independent from the others. Then fit linearly in the projected two dimensional spaces of position and time: $x - t$, $y - t$ and $z - t$, where t , the time of the corresponding hit, is the independent variable. This way, the problem is reduced to fitting the equation $y = c_1x + c_0$ in each position and time space as seen in Figure 5.5. From here apply χ^2 minimization, which in the case of linear data fitting is exactly the method of least squares. In this

5.3. LIKELIHOOD

scenario, if the data points are defined as $(x_1, y_1), \dots, (x_m, y_m)$, then the solution that minimizes the χ^2 will be

$$\vec{c} = (X^T X)^{-1} X^T \vec{y}, \quad (5.9)$$

where

$$\vec{c} = \begin{bmatrix} c_0 \\ c_1 \end{bmatrix} \quad \& \quad X = \begin{bmatrix} 1 & x_1 \\ 1 & x_2 \\ \vdots & \vdots \\ 1 & x_m \end{bmatrix} \quad \& \quad \vec{y} = \begin{bmatrix} y_1 \\ y_2 \\ \vdots \\ y_m \end{bmatrix}. \quad (5.10)$$

Once \vec{c} is computed for each position and time space, the vertex position is estimated to be at $(c_{0,x}, c_{0,y}, c_{0,z})$ with direction $(c_{1,x}, c_{1,y}, c_{1,z})$, where the second subscript denotes the spatial component of the data that was used in the fit.

5.3 Likelihood

A more robust technique for reconstructing potential muon tracks is a Maximum Likelihood Estimate [51]. In essence this is a statistically–driven parameter fitting technique that allows for more complex modelling, such as the inclusion of the VC emissions. Specifically, if the i^{th} DOM observes data \vec{x}_i , then the probability of observing this data given track parameters $\vec{\theta}$ is described by a probability distribution $p(\vec{x}_i | \vec{\theta})$. Since this is true for each DOM in a given event, the likelihood distribution is defined as

$$\mathcal{L}(\vec{\theta}) = \prod_{i=1}^n p(\vec{x}_i | \vec{\theta}), \quad (5.11)$$

where the indices are over all n DOMs. The data, \vec{x} , can carry information such as the times, charges, and directionality of the hits. The varied parameters, $\vec{\theta}$, carry

5.3. LIKELIHOOD

the information about the track including the direction, the vertex, the vertex time, and the energy. The parameters that maximize the distribution $\mathcal{L}(\vec{\theta})$ are the best estimates for the track given this method.

Finding this maximum is generally non-trivial and a difficult problem. Computational limits motivate using more robust maximization techniques than full parameter searches, and generally these are techniques that use gradient driven methods. Due to this methodology, generally the solution proposed by the MLE is not the global maximum, and is usually a local maximum. The result of the maximization is thus heavily dependent upon the initial conditions and the exact method of fitting.

5.3.1 Likelihood Function

Though the general theory for how the likelihood function will turn out is understood, an explicit form for $p(\vec{x}_i|\vec{\theta})$ is still required. This probability function could be made arbitrarily complex by attempting to account for every physical detail, so the assumptions and physical processes that will be modeled need to be stated. The next step would be to account for the scattering and absorption of light using the geometric time and direct distance that the emitted photon would travel before hitting the DOM given a guess track. This seems like a small change, but has large repercussions in the probability distribution describing the data given a hypothesis track. IceCube uses the Podel function [52], which explicitly takes the following form,

$$p(t_{\text{res}}|\vec{\theta}) = \frac{1}{N(d)} \frac{\tau^{-d/\lambda} \cdot t_{\text{res}}^{d/\lambda-1}}{\Gamma(d/\lambda)} \cdot \exp\left(-t_{\text{res}} \cdot \left(\frac{1}{\tau} + \frac{c_{\text{medium}}}{\lambda_a}\right) - \frac{d}{\lambda_a}\right),$$

$$N(d) = e^{-d/\lambda_a} \cdot \left(1 + \frac{\tau \cdot c_{\text{medium}}}{\lambda_a}\right)^{-d/\lambda}, \quad (5.12)$$

5.3. LIKELIHOOD

where d is the photon travel distance, λ is the scattering length, λ_a is the absorption length, $\Gamma(x)$ is the Gamma function, c_{medium} is the speed of light in water, and τ is an inverse time parameter for fitting [52]. Given these parameters, which are physically motivated or fit using simulated data, the Pandel function gives the probability of observing a residual time for a hypothesis track. It is important to note here that $\vec{\theta} = (\vec{v}, \vec{x}, t_{\text{vertex}})$, where we have the track direction, vertex position and vertex time respectively.

The Pandel function favours positive residual times, so much so the probability has varying behaviours as $t_{\text{res}} \rightarrow 0$. Figure 5.6 shows this behaviour over three different distances over a domain for 300 nanoseconds in residual time. As the distance is increased for the emission point, the probability of observing a photon later than expected increases. This is consistent with the concept of the probability of light being absorbed or scattering increasing as the distance increases.

5.3. LIKELIHOOD

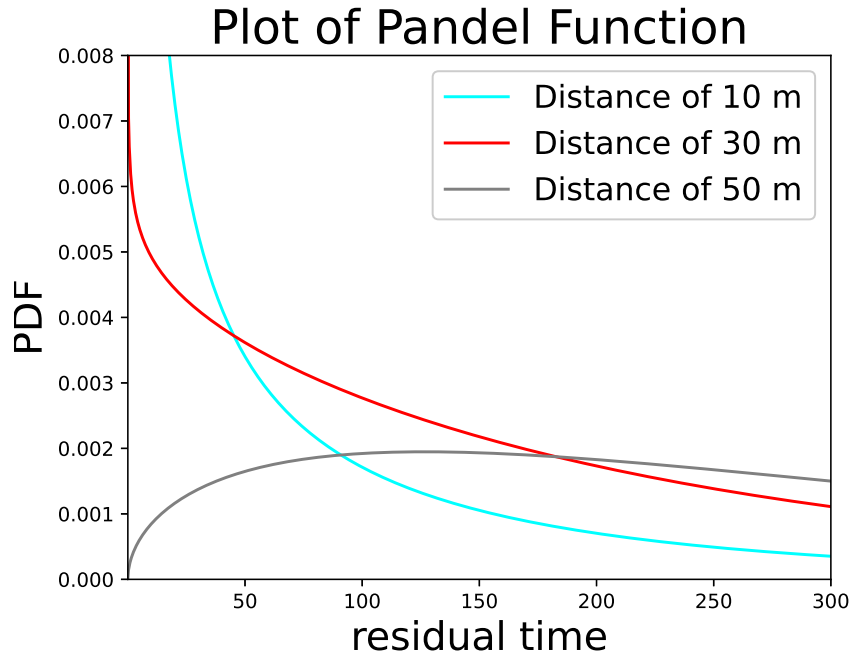


Figure 5.6: A figure showing a plot of the podel function over 300 nanoseconds with 10 meters, 30 meters and 50 meters of travel for the emitted light. The fit parameters, including λ_a and λ_s , are fit according to the IceCube parameters as described in [52].

Theoretically this probability distribution should describe the behaviour of light in water, once the parameters have been fit accordingly. This, however, is not the case practically. The issue arises particularly with the behaviour around $t_{\text{res}} = 0$, since in real data there are statistical fluctuations due to uncertainty in data collection. By ignoring the detection step of the process, the Podel function can't effectively model the data as one would actually observe it, and for this reason the detector error needs to be folded into the function.

The simplest model for detector error is a gaussian, and a known method of folding this error into the Podel function is a convolution, as done here [55]. The gaussian width can then be fit and altered to account for any time jittering caused

5.3. LIKELIHOOD

by detection limitations thereby allowing for negative time residuals. If, as in [55], the pandel function is reparameterized as $p_{\text{pandel}}(\rho, \xi, t)$ from $p_{\text{pandel}}(\vec{v}, \vec{x}, t)$, then the convolution with a gaussian of mean zero and standard deviation σ is given by

$$\mathcal{F}_\sigma(\rho, \xi, t) = \int_0^\infty \frac{dx}{\sqrt{2\pi\sigma^2}} p(\rho, \xi, x) e^{-(t-x)^2/2\sigma^2}. \quad (5.13)$$

This integral has an exact form [55],

$$\mathcal{F}_\sigma(\rho, \xi, t) = \frac{\rho^\xi \sigma^{\xi-1} e^{-t^2/2\sigma^2}}{2^{(1+\xi)/2}} \left[\frac{{}_1F_1(\frac{1}{2}\xi, \frac{1}{2}, \frac{1}{2}\eta^2)}{\Gamma(\frac{1}{2}(\xi+1))} - \sqrt{2}\eta \frac{{}_1F_1(\frac{1}{2}(\xi+1), \frac{3}{2}, \frac{1}{2}\eta^2)}{\Gamma(\frac{1}{2}\xi)} \right], \quad (5.14)$$

where

$$\eta = \rho\sigma - \frac{t}{\sigma} \quad (5.15)$$

and ${}_1F_1$ is the confluent hypergeometric function [55]. Fortunately ${}_1F_1$ is available in multiple computing languages and allows for numerical evaluation of $\mathcal{F}_\sigma(\rho, \xi, t)$ [55], where there is a plot over an example domain in Figure 5.7. This is still non-trivial due to convergence bounds on ${}_1F_1$, and as in [55] approximations for different domains must be used in order to accurately be able to use the entire distance and time domain. For the exact approximations used, refer to [55], but the regions that need to be approximated will be discussed. In [55], the regions are described using the ξ and η parameters, but it is easy enough to translate these to t and d . The regions used for this reconstruction are adapted from [55].

5.3. LIKELIHOOD

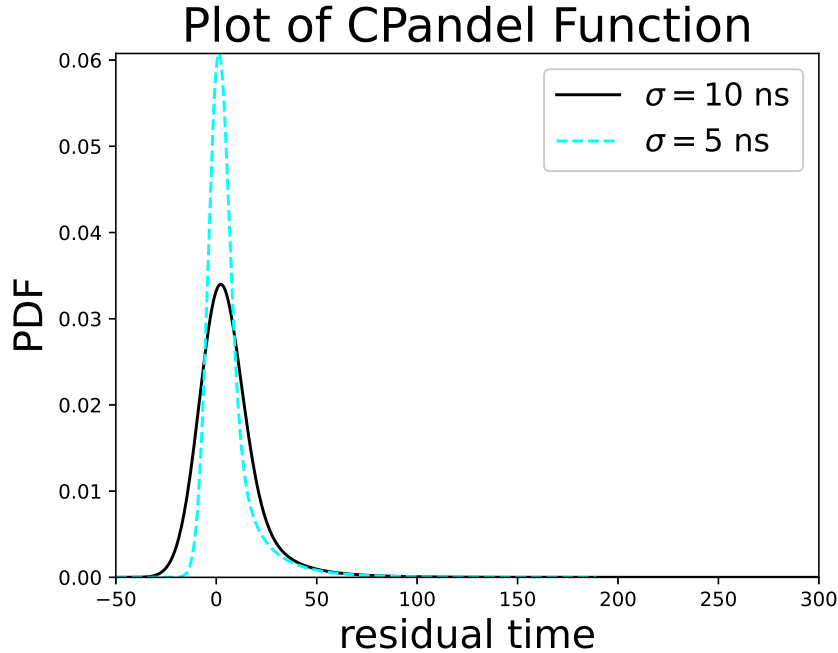


Figure 5.7: A figure showing a plot of the CPandel function over -50 ns to 300 ns at 50 meters of travel distances for the emitted light. The parameters aside from σ are fit according to the simulated data, and we have two plots of $\sigma \in \{5 \text{ ns}, 10 \text{ ns}\}$.

The simplest regions to understand are the unlikely regions. These are the ones in which it is incredibly unlikely to find any events as the residual time is either very positive ($t_{\text{res}} > 3500 \text{ ns}$), or too negative ($t_{\text{res}} < -25\sigma \text{ ns}$). In these regions, independent of distance, these residual times are unphysical and hence heavily penalized by this likelihood. The next region we consider is for $-5\sigma < t_{\text{res}} < 30\sigma$ and $d < 5\lambda_s$. This describes the most common region for events to occur, and is within the convergence boundary of the hypergeometric functions. The exact form of the equation, as described in Equation 5.14, is the one taken for this region and promotes the general expected behaviour around the peak. The remaining regions are a combination of the possible ranges of distance and time; there are approximations for large t and

5.3. LIKELIHOOD

small d , small t and large d and large t and large d . These regions each have various approximations associated. The approximations are omitted here but can be found in [55].

5.3.2 Function Fitting

In order to use the CPandel distribution, the fitting parameters need to be found such that they match the simulated data. We can see a distribution of the residual times computed over thousands of events in Figure 5.8. Due to the lack of simulated background and noise but instead an artificial Gaussian smearing the resulting distribution is quite smooth and idealized. Moreover, the data is normalized and hence the values on the y -axis represent the percentage of the total number of events that fit this criteria.

The data in Figure 5.8 is over all distance ranges of the produced light, but the CPandel function clearly depends on the distance as seen in Equation 5.14. Thus, it is useful to fit to the simulated data by categorizing over different distance ranges, which can be visualized in similar plots to Figure 5.8. In particular, these plots can be seen in Figures 5.9, 5.10, 5.11 and 5.12, where the range shifts incrementally upwards over these four figures. With the residual time separated by distance, it is clear to see the dependence that it has on the distance, and hence the importance of fitting over all of the viable distance ranges of light that will be detected. The prominent feature is a general flattening of the distribution for larger distances, which is expected as light has a higher chance of scattering/being absorbed the further it travels.

5.3. LIKELIHOOD

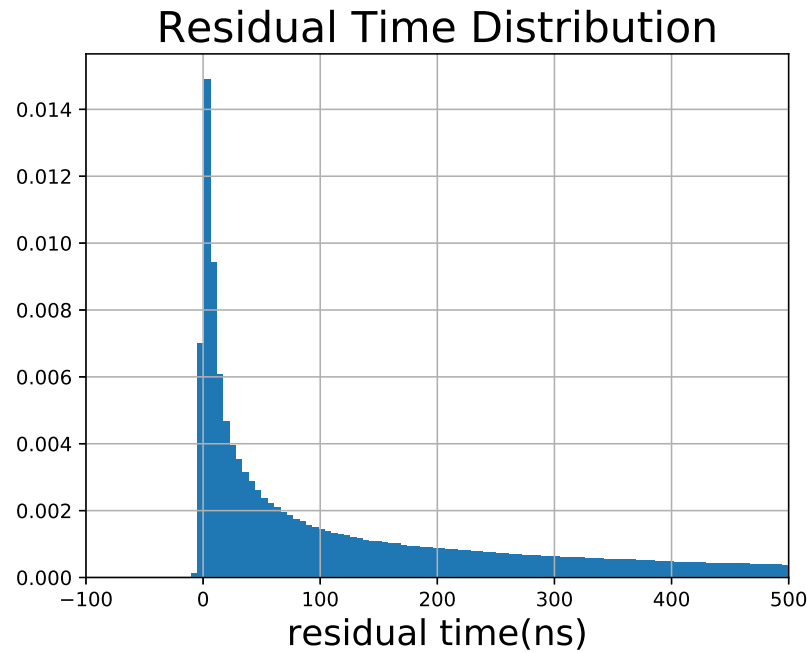


Figure 5.8: Normalized residual time distribution made using simulated events. Here the residual time is computed by comparing the geometric time with the true travel time simulated by the photon propagation software. This does not contain any dark noise or electronic noise and hence is an idealized distribution.

5.3. LIKELIHOOD

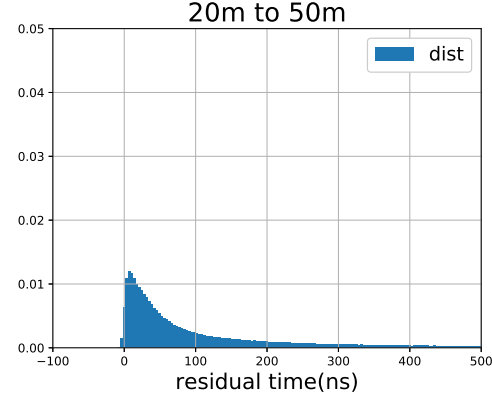
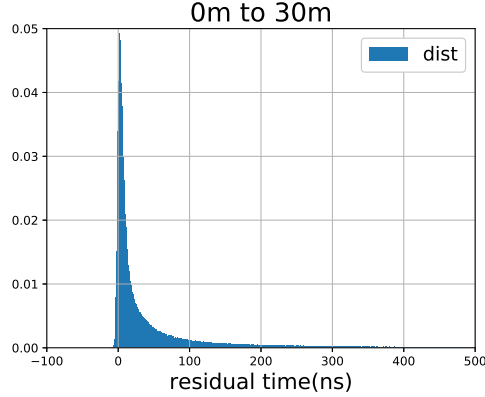


Figure 5.9: Distances from 0 to 30 meters.

Figure 5.10: Distance from 20 to 50 meters.

Figure 5.11: Distances from 40 to 70 meters.

Figure 5.12: Distances from 60 to 90 meters.

Figure 5.11: Distances from 40 to 70 meters.

Figure 5.12: Distances from 60 to 90 meters.

Figure 5.11: Distances from 40 to 70 meters.

Figure 5.12: Distances from 60 to 90 meters.

5.3.3 Other Potential Distributions

The CPandel isn't the only option for a likelihood distribution. Another natural choice would be to use real data to emulate a distribution. As was discussed in Section 3.3, STRAW has been collecting data since 2018 in order to get a measurement on the attenuation length and could in theory provide data for such a use. Figure 5.13 provides an example of such a plot. It is not immediately clear why such a setup should provide a distribution like one expects from functions like the Pandel and

5.3. LIKELIHOOD

CPandel. The variable plotted in the Pandel and CPandel is the residual time, and for the data we have only plotted the arrival time of light. However, as the driving agent in the distributions is the scattering of light, the arrival time in the STRAW data will naturally observe a smearing due to this phenomena. In this way, the arrival time mimics the behaviour of the residual time, which is the difference between the observed and geometric times.

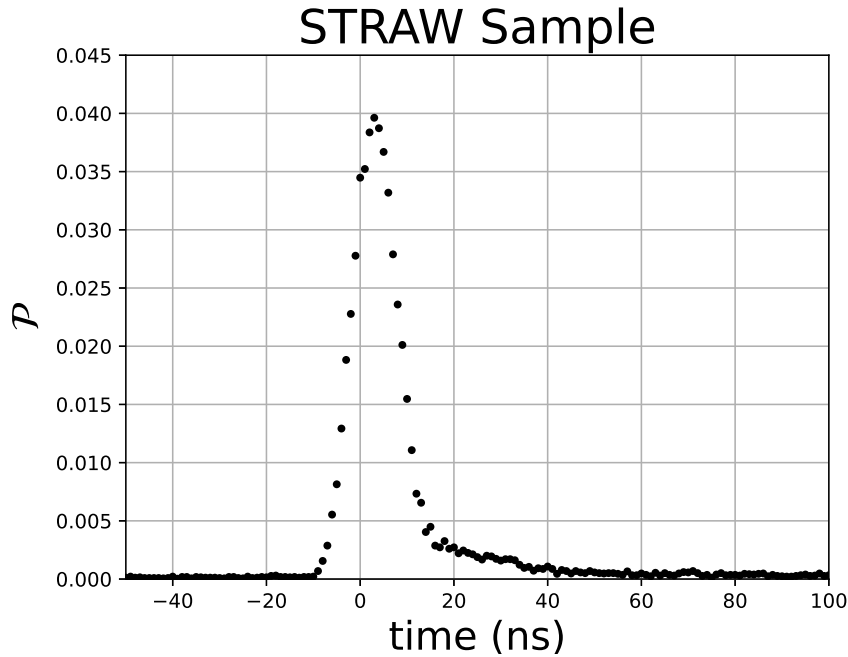


Figure 5.13: A snippet of data stacked over multiple channels using a POCAM flash as a source of light. The POCAM provides a 10 ns flash of light, and sits at a fixed distance from the Optical Module. The time has been shifted for convenience.

This isn't immediately usable as a distribution. Due to the sampling rate and limitations of the detector, there will be gaps between plot points, and these gaps do not work when times can go between these values. The first thing to try is a simple interpolation to fill these gaps. Consider linear and cubic interpolation as

5.3. LIKELIHOOD

shown in Figures 5.14 and 5.15 respectively. These both do the job of filling the gap between the points, as interpolations do, but they have varying results. The linear interpolation results in a piecewise fit that isn't very smooth, which can be an issue when using gradient decent methods of fitting as the likelihood space built using this distribution will also be constructed in a piecewise manner. This issue is slightly resolved with a cubic interpolation, however the issue becomes more exacerbated in the end and beginning tails of the distribution where the data becomes more noisy. The interpolation attempts to continue fitting between the points even as noise begins to dominate, and can result in a plethora of oscillations in the fit. These fluctuations are also quite bad for the minimization as they can introduce more minima that could trap the minimizer.

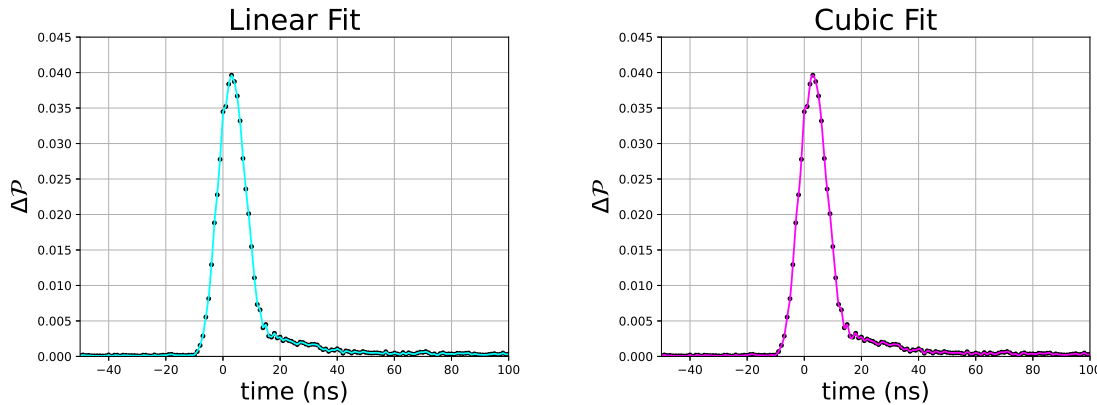


Figure 5.14: Linear interpolation of the STRAW data. This produces a likelihood distribution that has piecewise behaviours due to the linear nature.

Figure 5.15: Cubic interpolation of the STRAW data. The cubic fit allows for a smoother fit between points, but still has a piecewise nature due to the interpolation.

To deal with the noise that is occurring near the tails of the distribution a filter can be applied to smoothen the data. In particular, the Savitzky-Golay filter is a

5.3. LIKELIHOOD

digital filter method to help remove the jagged edges in the target function [48]. This filter is applied to the STRAW data in Figure 5.16, where the effect becomes clear. Compared to the interpolations in Figures 5.14 and 5.15, the Savitzky-Golay filter is clearly a smoother fit. The tail jittering still tends to cause the distribution to shift erratically, but odd variations like at the zero nanosecond count are smoothed out.

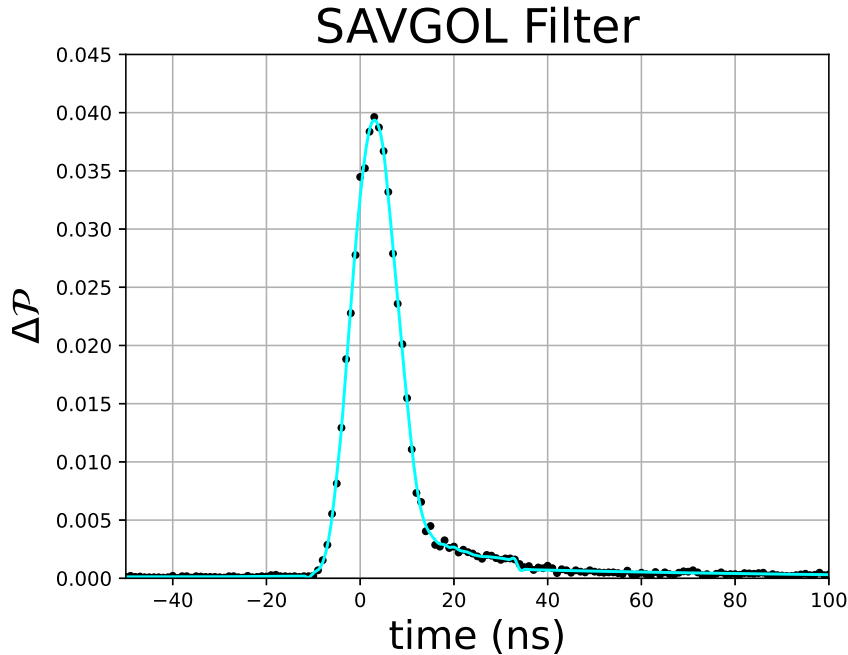


Figure 5.16: A data filtering method to help remove the background noise that is present in the STRAW data.

After having seen the fits in Figures 5.16, 5.14 and 5.15 there is still a glaring issue that has not been accounted for; these fits do not account for varying distances. Due to data collection limitations from the geometry of STRAW, getting a broader range of distances is impossible. Without being able to account for the distance dependence on the residual time distribution this method is limited. Being able to poll different distances and interpolate these distributions could be useful.

5.3. LIKELIHOOD

A method that could account for this would be using an explicit equation rather than a fit. A distribution that looks similar to the residual time distribution is the exponential gaussian. Referring to Figure 5.17, varying the two parameters can change the distribution to mimic the distance dependence. The issue then becomes to find a relationship between these values and the effect the distance has on the distribution. This is non-trivial, and as there are already forms of the CPandel that do this with physical motivations, there isn't too much benefit in pursuing this unless there is more real data to build this relationship with.

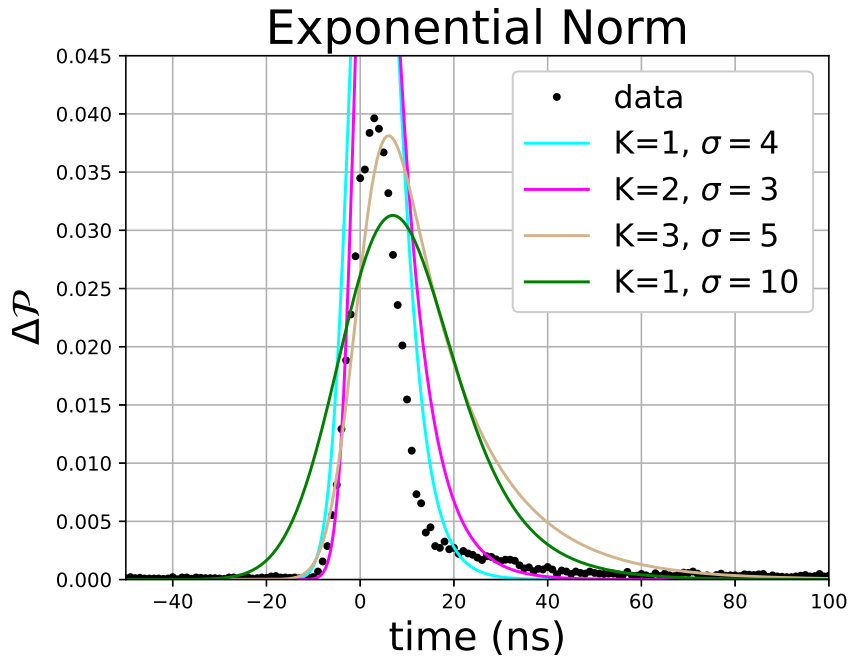


Figure 5.17: Varying exponential normal/gaussian distributions compared to the STRAW data.

5.4. TRACK FITTING

5.4 Track Fitting

With the track parameterization understood, a likelihood distribution in the form of the CPandel function, it is now at a point where the reconstruction step can actually take place. As a likelihood, $\mathcal{L}(\vec{\theta})$, for a given track gives a probability, we wish to maximize this function with respect to $\vec{\theta}$. In order to computationally accomplishing this goal, the first step is to utilise a standard method in maximizing likelihoods by taking the logarithm,

$$\ell(\vec{\theta}) = \log \left(\mathcal{L}(\vec{\theta}) \right) . \quad (5.16)$$

As we recall the form for $\mathcal{L}(\vec{\theta})$ in Equation 5.11 is a product of probability distributions, then naturally we see

$$\ell(\vec{\theta}) = \sum_{i=1}^n \log \left(p \left(\vec{x}_i | \vec{\theta} \right) \right) , \quad (5.17)$$

which is now a sum rather than a product. This will immediately be more useful as computationally it is easier to take a sum then a product. Another point to note is that generally one finds the minimums of functions rather than maximums purely due to convention, and so generally the minima of $-\ell(\vec{\theta})$ is what is computed.

For the actual minimization process, the common method is to use a simplex based technique [47]. This method, sometimes referred to as the Nedler-Mead algorithm, is powerful for finding local minima of multi-parameter systems and uses an approach that does not rely on derivatives. The benefit is that this method is relatively straight forward and easily implemented. A more robust technique is to use a gradient based approach, such as the nonlinear conjugate gradient method [21], which uses a gradient to determine the direction in which the minimizer will head. The benefit to this latter

5.5. CORRECTIONS

approach is that it is more consistent and reliable in finding the minima.

Ultimately the choice of minimization technique is case dependent and can vary. Both of these are compared in the analysis.

5.5 Corrections

Through some testing and debugging, it was found there were some manual corrections and changes that had to be made to observe an improvement in the likelihood reconstruction. These changes included reparameterizing the problem into a spherical coordinate-like form, and an extra penalty on the likelihood for negative residual values.

5.5.1 Reparameterizing

Due to the seed for the likelihood fit being parameters resulting from the linear fit, the resultant minimization can vary depending upon how well the original fit does. A flaw of the linear fit method is that the vertex fit is not physically meaningful, and doesn't serve any other purpose in this initial fitting technique. This can occasionally result in a vertex that is very far away from the director, which can have drastic effects on the minimization. In particular, the further the vertex is from the detector the more sensitive the minimizer is to changes in the direction azimuth and zenith angles. This can impede the minimization process, and cause the minimizer to miss even local minimas.

To avoid these potential issues, the problem was reparameterized from $\vec{\theta} = (\theta, \phi, \vec{x}, t)$ to $\vec{\theta} = (\theta, \phi, \vartheta, \varphi, t)$. The new ϑ and φ refer to the zenith and azimuth angles that point to the vertex at a fixed radius r related to the size of the detector. Fixing r

5.5. CORRECTIONS

determines a sphere around the center of the detector, and the intersection of the track with that sphere is determined and the new vertex is determined to be the first point that intersects the sphere, which allows for computation of these new angles. If the line does not intersect the sphere, the event is determined to be outside the detector and would be disregarded in event cleaning anyways.

5.5.2 Extra Penalty

As the likelihood function represents the ideal residual time distribution, the goal of the likelihood method is to generally push the distribution towards the CPandel distribution. This is a vague approximation of how the likelihood method actually works, but it motivates penalizing negative residual values even more. Occasionally the minimization process won't find a distribution that fits the CPandel well, and in these cases adding an extra artificial presence to nudge the residual time distribution in the right direction can improve the fit.

Though this solution works, it is inherently temporary and is a band-aid method to force the likelihood minimization to behave the way we want. Ideally the likelihood distribution would be robust enough to correctly push the minimization in the correct direction without this manual push.

Chapter 6

Results

Having constructed the theory of the physics and computation, we are in a position to discuss the results that come about from these reconstruction efforts. To discuss these results, we consider the methods in which a reconstruction technique can be considered successful. The easiest, and most useful parameter to check is the direction. Comparing the reconstructed direction with the true direction is done by computing the solid angle between the directions. Computing this is simple; suppose the reconstructed direction is \vec{u} and the true direction is \vec{v} , then the solid angle is

$$\alpha = \arccos(\vec{u} \cdot \vec{v}) , \quad (6.1)$$

where we are assuming the directions are normalized to unit length. This solid angle can then be used to fill a histogram of a large number of trials to build a distribution.

6.1 Linefit

The simplest method for reconstruction that has been discussed is the linear fit using the method of least squares. In figure 6.1 we see that this method provides a pretty

6.2. LIKELIHOOD

decent first guess for a direction. The angular resolution seems to peak around a three degree resolution, and slowly falls off as we get further away from the truth.

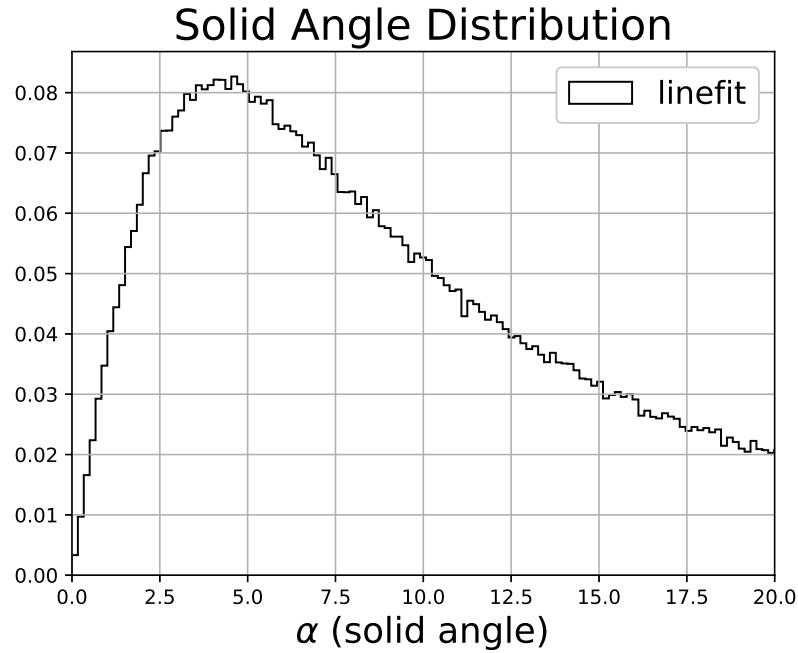


Figure 6.1: A distribution of the solid angles for reconstructed and true directions using the linefit method. The solid angle is given in degrees for clarity.

The quality of this reconstruction will inevitably affect the quality of the following reconstruction step, and as such should not be ignored.

6.2 Likelihood

We can make a similar plot for the angular distribution of the reconstructed angle using the linefit as a seed to the likelihood algorithm. Looking at figure 6.2 we see how well the likelihood reconstruction performs when using the linefit as a seed, but also how it compares to a perfect starting point, the true track information.

6.2. LIKELIHOOD

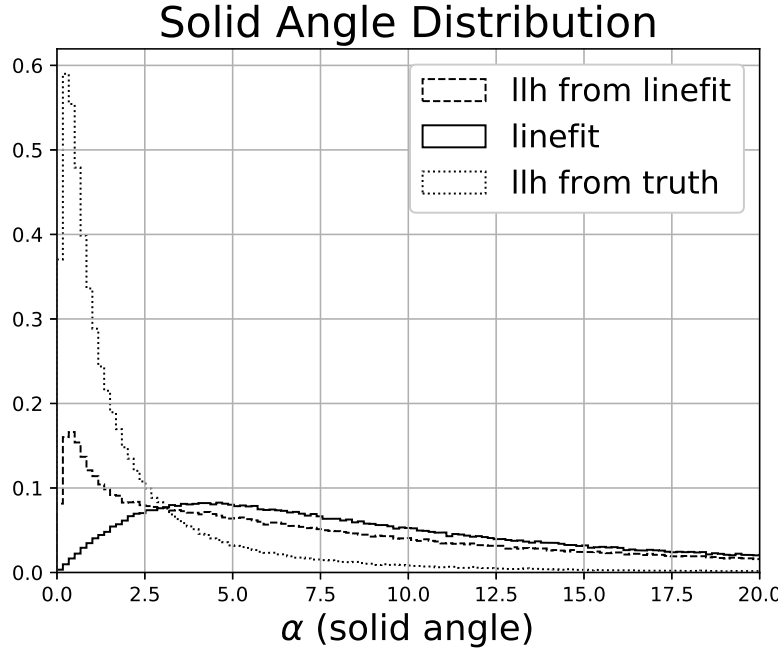


Figure 6.2: A distribution of the solid angles for reconstructed and true directions using the likelihood method. The linefit reconstruction angular resolution is also plotted alongside a distribution for the likelihood given the true track as a starting point.

Figure 6.2 shows us that with perfect information, the likelihood reconstruction does pretty well. This effectively shows the upper limit to the performance of the reconstruction as it is, but also shows that there is plenty of room for improvement when starting at the linefit seed. It is relatively standard for reconstruction techniques to be highly dependent upon the initial conditions, as the technology used boils down to being a minimization of a multiparameter space. This effect is in full swing when we compare the two starting conditions, which emphasizes that another path to improving the reconstruction would be to improve the initial guess.

This resolution plot can also be represented by plotting the difference in the directional coordinates. As the directions are length one, we can separate the azimuthal (ϕ)

6.2. LIKELIHOOD

and zenith (θ) errors. Then, plotting the difference between the true azimuth/zenith and the reconstructed azimuth/zenith leads to figure 6.3.

Direction Angular Difference

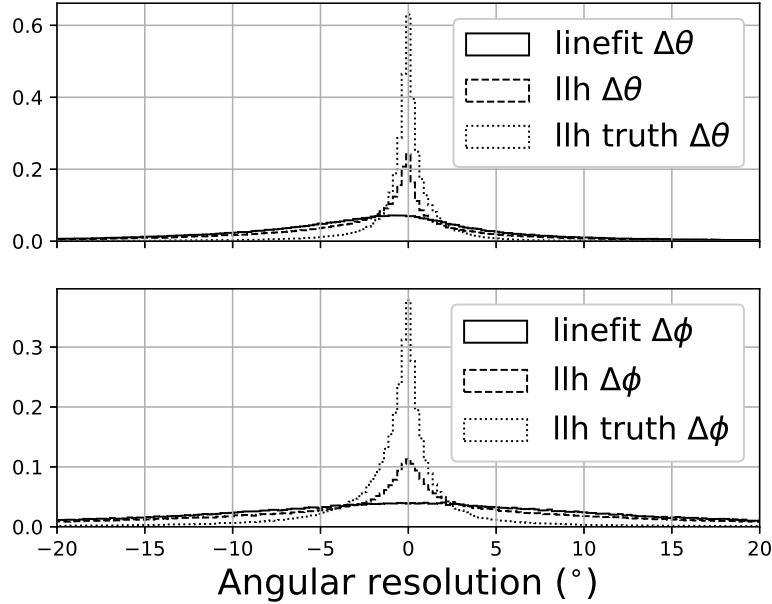


Figure 6.3: A distribution of the solid angles for reconstructed and true directions using the likelihood method separated into zenith and azimuth components in degrees. **Above:** The zenith component distribution where $\Delta\theta = \theta_{\text{true}} - \theta_{\text{reco}}$ in the reconstruction process. **Below:** The azimuth component distribution where $\Delta\phi = \phi_{\text{true}} - \phi_{\text{reco}}$ in the reconstruction process.

The reconstruction still shows a similar shape that that observed in figure 6.2, as clearly the angular resolution is highly initial condition dependent. There is something of note in the zenith plot though (θ), as there is a slight skewing towards negative $\Delta\theta$ values when using the linefit. This is due to the way the detector is simulated, since the current setup assumes IceCube-like DOMs which only face downward. As linefit is ignorant to the actual method in which light is emitted from the track, this introduces a degeneracy in the fit that can push linefit towards a particular direction.

6.2. LIKELIHOOD

	$\Delta\theta(^{\circ})$		$\Delta\phi(^{\circ})$	
llh type	μ	σ_s	μ	σ_s
line	-1.89	7.21	-0.01	9.52
default	-1.47	6.32	-0.002	8.41
true	-0.28	2.74	-0.62	4.18

Table 6.1: Some simple statistics on the data distributions in Figure 6.3. Here ‘**line**’, ‘**default**’ and ‘**true**’ refer to just the linear fit, the likelihood using the linear fit as the seed, and the likelihood using the truth as a seed fits respectively. The means (μ) are computed in the standard way, but the standard deviation (σ_s) is the sample standard deviation, and hence is normalized by a factor dependent upon the sample size.

The resolution in the zenith angle seems to be slightly better than that of the azimuthal, which can be attributed to the geometry of the detector. In particular, the current geometry assumes vertical lines of detectors, which would expectedly perform better. These plots are in fact excellent for attempting to understand the effects of the geometry of the detector. Referring to Table 6.1 the difference in the accuracy of the azimuthal to the zenith becomes clear. The zenith has a consistently reduced sample standard deviation over all three methods of fitting, with subsequent techniques improving on the previous. The interesting values to note are all of the means being negative. These negatives aren’t as substantial for the values that are closer to zero, like the means in $\Delta\phi$. The means in $\Delta\theta$ do tend closer to zero as the techniques “improve”, however the substantial shift in the linefit mean is an artifact of the method of simulation used. As the DOMs have been simulated in a manner similar to that of IceCube, they are all downward facing and bias the linear fit to be consistently fit more horizontally than the truth, as a negative sign implies the

6.2. LIKELIHOOD

reconstructed azimuthal is larger than the true azimuthal. This bias should in theory vanish if upward facing DOMs were to be included, but that is something to be considered as a part of the detector geometry.

To test which initial parameter most affects the reconstruction, I started the reconstruction seed from two different initial states; fixing the starting vertex at the truth, and fixing the starting direction in the true direction. Using these initial conditions, a plot similar to figure 6.2 could be created, and is in figure 6.4. As can be seen from the legend, there are a couple of variable seeds in this distribution, and the results seem to point towards the vertex resulting in the largest improvement in the resolution. This can come off as a bit surprising, especially when the parameter that is being plotted against is the direction resolution. The improvement does tell us where we need to improve the initial guess, and focusing on an improved vertex for the initial seed seems to be the way to go.

6.2. LIKELIHOOD

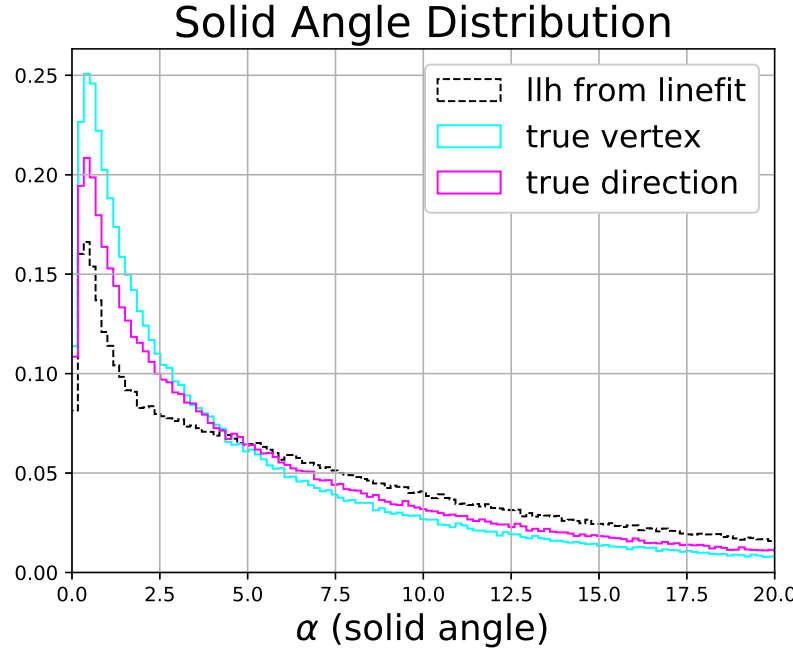


Figure 6.4: Similar to the distribution in figure 6.2, the angular resolution is plotted in degrees into a histogram. Here the initial starting conditions are grouped into the true vertex, true direction and only linefit, where the former are given linefit parameters for the remaining parameters.

To get a better idea of how the plots in Figure 6.4 and Figure 6.2 compare, we can make a simple table to look at the percentage of events that are below certain cut-off angular resolution values. In Table 6.2 we see these exact percentages for angular resolutions below 0.1° , 0.5° , 1° , 5° , and 10° from the true direction. Comparing the values, we see that the largest relative increases in the percentages seem to occur between linefit and the standard likelihood reconstruction and going to the likelihood reconstruction using the truth as a seed. Looking at the resolutions below 0.1° , 0.5° , and 1° the percentage of events increase by an order of magnitude between linefit and the standard likelihood method. This same jump occurs again when getting to the likelihood reconstruction using the truth as a seed.

6.2. LIKELIHOOD

α	0.1°	0.5°	1°	5°	10°
line	0.02	0.39	1.54	24.25	50.76
llh	0.47	5.67	11.43	38.02	59.58
llhdir	0.69	7.60	15.70	50.11	70.54
llhvert	0.71	8.99	19.23	57.65	76.31
llhtrue	2.70	25.03	45.21	86.92	96.29

Table 6.2: The labels ‘line’, ‘llh’, ‘llhdir’, ‘llhvert’, ‘llhtrue’ refer to the linefit, likelihood, likelihood using the true direction seed, likelihood using the true vertex seed and likelihood using the truth as a seed reconstructions respectively. The values are given in percentage of events below the given α solid angle to the true direction.

As the largest increase in accuracy occurs from changing the vertex position, as seen in Table 6.2, a comparison of the vertex positions given by the linear fit with the true vertex positions might provide some insight into why this is so. This is a non-trivial comparison, as the vertex position has three free variables, and projecting along a single axis isn’t particularly useful due to the nature of the linear fit vertex occasionally ending up very far away from the detector. For this reason, a useful representation is one similar to that of Figure 6.3, as in the process of reconstructing, the vertex is projected onto a sphere anyways. Thus, assuming this projection of the vertices, the problem reduces to looking at the angle distribution in the zenith (θ) and azimuth (ϕ). Figure 6.5 shows what this distribution looks like compared with the true vertex distribution.

6.2. LIKELIHOOD

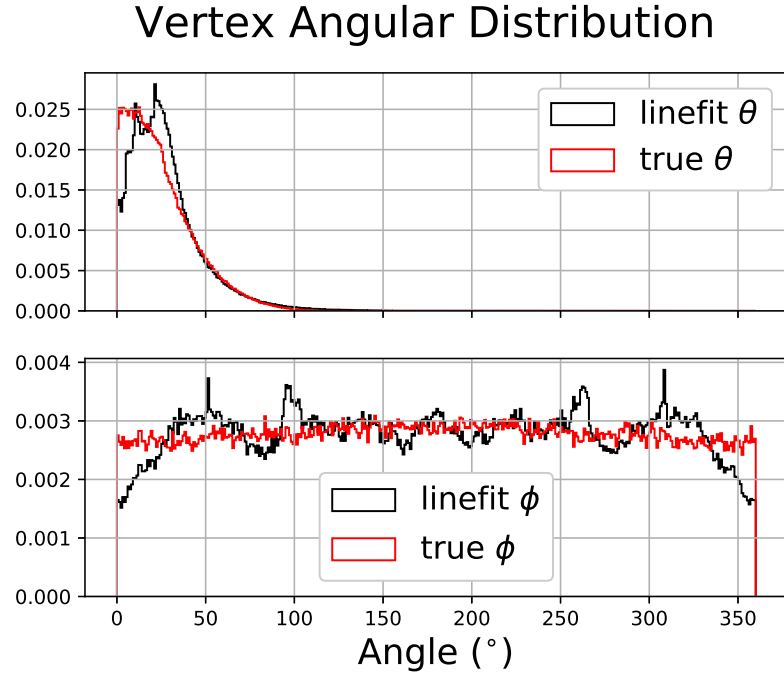


Figure 6.5: A distribution of the vertex zenith and azimuthal components when projected onto a sphere of radius 550 meters. **Above:** The zenith component distribution. **Below:** The azimuth component distribution.

The shapes of the plots in Figure 6.5 are telling. The top plot, the zenith distribution, is heavily pushed up to angles around zero for good reason. The simulated muons are primarily cosmic, and hence the vertex being primarily in the $[0, 50]$ degree range makes sense. The lack of angles in the symmetric part near 360 are due purely to the branch choice as generally for spherical coordinates $\theta \in [0, 180]$ degrees since the complement angle is covered by the azimuthal angle. The more valuable point is the difference in the linear fit zenith distribution with the true distribution. The true distribution is consistent with a cosmic muon source, but the linear fit seems to be dragging the vertex positions towards two particular peaks. These peaks can be seen in the zoomed plot made in Figure 6.6 to be around 10 and 22 degrees. These angular peaks can be explained as the vertices tending to bunch up near the DOM

6.2. LIKELIHOOD

locations. If the source of muons was isotropic, and not just cosmic, one could expect this pattern to repeat throughout the domain of the zenith. To understand why these peaks occur, it is simplest to think of a zenith distribution as a projection along the azimuthal angle. Unlike simple cartesian projections, which are usually onto a plane in three dimensions, this is a projected onto a rotating surface. The result is a stacking of the azimuthal dependence, leaving only the distance between the DOMs.

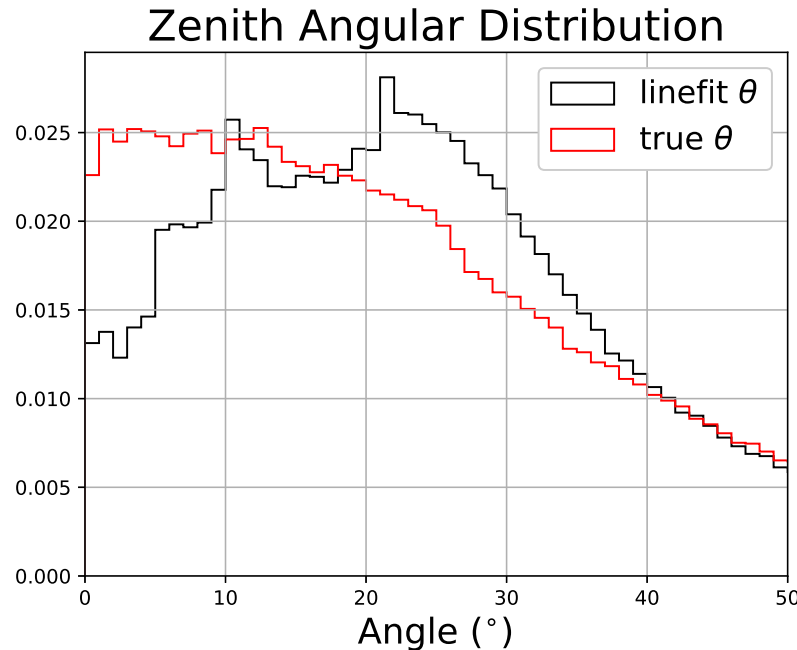


Figure 6.6: A distribution of the vertex zenith and azimuthal components when projected onto a sphere of radius 550 meters. **Above:** The zenith component distribution. **Below:** The azimuth component distribution.

On the other hand, the azimuthal spans its full range of $[0, 360]$ degrees. The true vertex azimuth can be observed as being relatively uniform, yet the linefit reconstructed vertex has a clear oscillatory pattern. Similar to the peaks observed in the zenith distribution, these can be attributed to the DOMs where here the projection along the zenith leads to the distance between the lines of the DOMs being the active

6.2. LIKELIHOOD

agent. Both the azimuthal and zenith distributions show that the linear fit has an inherent bias towards the locations of the optical modules, and removing this bias could improve the vertex reconstruction which would in turn improve the likelihood reconstruction as seen in Figure 6.4.

We can also check whether there is a correlation with the likelihood values and the reconstructed angular resolution (α). To do so, we need a way to include both the final and initial likelihood values, as there can be a wide variety of ranges that a reconstruction can start and end at. For this reason, we consider plotting the ratio between the final negative loglikelihood value and the initial, ℓ_f/ℓ_i . Thus, a smaller value denotes a larger improvement in the likelihood value. On the other hand, any value above one denotes a drop in quality of fit. This plot is made in figure 6.7.

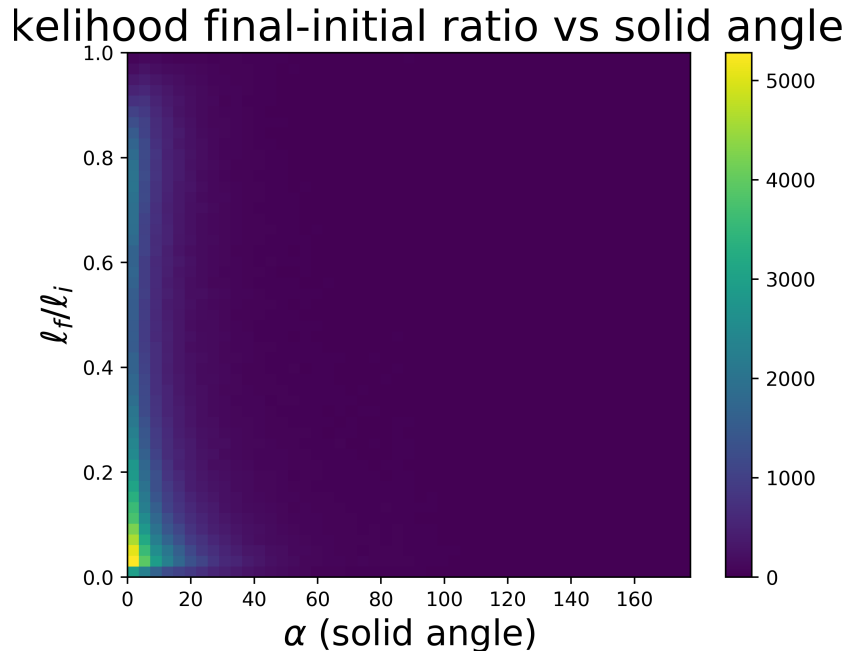


Figure 6.7: We plot the likelihood ratio ℓ_f/ℓ_i against the final reconstructed angular resolution using a heatmap.

6.2. LIKELIHOOD

Referring to figure 6.7, we see that the events are bunching up near a small ratio of ℓ_f/ℓ_i and small error in the solid angle α . This could point to a correlation between the increase in the quality of the fit and the increase in the directonality of the reconstructed track. There could still be some hidden biases here that are being unaccounted for, such as reconstruction angles that begin close to the truth only changing in small amounts but having massive likelihood value swings. For this reason, we need to check for sure that there are no hidden biases in both ℓ_f against ℓ_i and α_f against α_i .

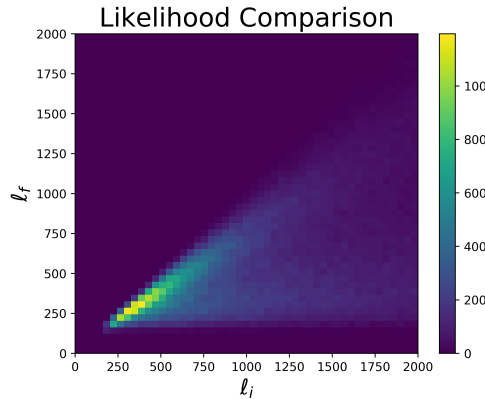


Figure 6.8: Correlation heatmap between the initial negative loglikelihood value and the final negative loglikelihood.

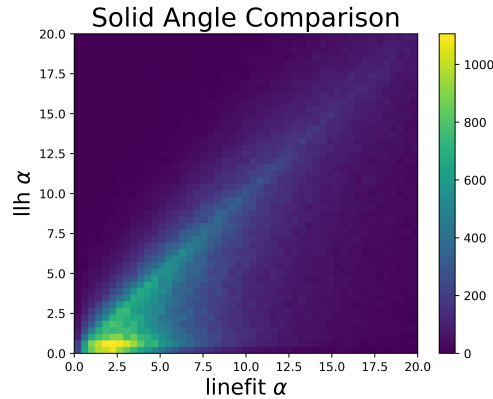


Figure 6.9: Correlation map of the final reconstructed angular resolution and the initial angular resolution.

Looking at figures 6.8 and 6.9, we can see that the reconstruction is behaving as one would expect. For both plots, the $y = x$ diagonal line would symbolize neither improvement nor regression, and anything below would suggest improvement. In both figures majority of the points end up below this line encouraging the correlation between the reconstruction improving both the likelihood value but also the

6.2. LIKELIHOOD

reconstructed angular direction. For figure 6.8, the clustering of events shows a correlation between good seed events leading to well fit final fits. The further the seed events get from being good fits, the more spread the quality of the final fit becomes. A similar result can be seen with the angular resolution correlation plot in figure 6.9. A useful method to quantify these correlations is the Pearson Correlation, where a value of one is perfect correlation, and a value of negative one is of perfect negative correlation. Figure 6.8 gives a Pearson Correlation of 0.38 while Figure 6.9 gives a correlation of 0.93. These are interesting values as at first glance it may seem that the likelihood values have a clearer correlation than the solid angles, but the correlation values seem to tell another story. There is still clearly a positive correlation, but the reduced correlation value in the likelihoods is interesting, however the observations from before still stand as there are plenty of events that occur below the $y = x$ line.

Another important parameter to consider when looking at reconstructions is the time it takes to run. This can become increasingly important as there are massive amounts of potential events a detector can observe during its runtime, and being able to reconstruct them becomes an important potential bottleneck.

6.2. LIKELIHOOD

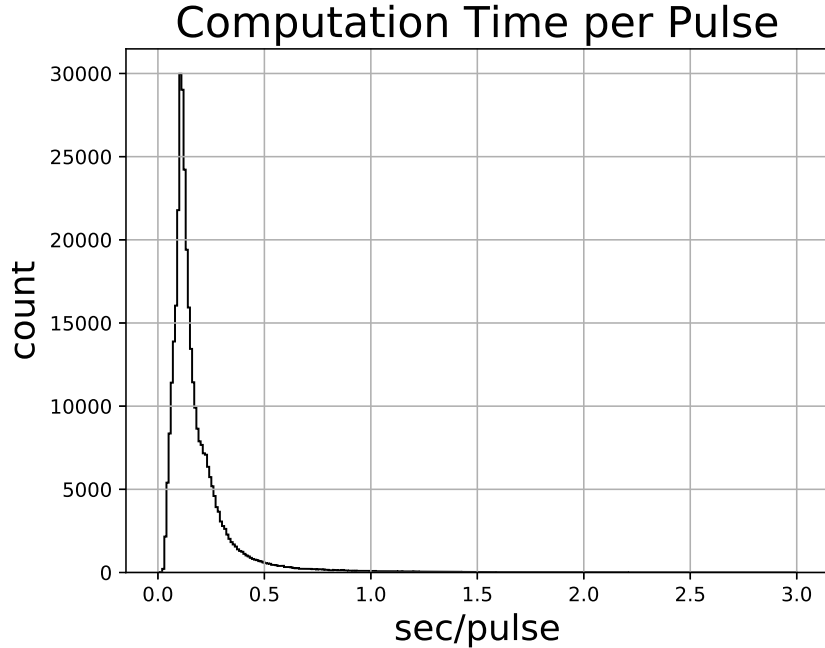


Figure 6.10: Distribution of the computation time for reconstructing events normalized by the pulse count. Higher energy events will naturally need to a larger number of observed pulses and increase the computation time accordingly.

Figure 6.10 plots the computation time for the reconstruction algorithm normalized by the pulse count, where the pulse count scales with the number of photons produced, and hence the energy of the muon. The peak occurs around 0.125 sec/pulse, which isn't great, though it is a decent first efficiency test. Ideally this will be sped up either by using clever techniques, or by shifting to a language like C++ where this repetitive nature of nested loops is better optimized. Parallelization schemes could also be introduced if even more speed up is required.

Chapter 7

Summary and Conclusions

7.1 Summary

7.2 Future Work

7.3 Conclusion

BIBLIOGRAPHY

Bibliography

- [1] Icecube documents. <https://software.icecube.wisc.edu/>.
- [2] Ocean networks canada. <https://www.pacific-neutrino.org/about-us>.
- [3] Mark Aartsen, Markus Ackermann, and et al. Neutrino emission from the direction of the blazar txs 0506+056 prior to the icecube-170922a alert. *Science*, 361(6398):147–151, 2018.
- [4] M.G. Aartsen, M. Ackermann, J. Adams, J.A. Aguilar, M. Ahlers, M. Ahrens, D. Altmann, K. Andeen, T. Anderson, I. Ansseau, and et al. The icecube neutrino observatory: instrumentation and online systems. *Journal of Instrumentation*, 12(03):P03012–P03012, Mar 2017.
- [5] R. Abbasi, Y. Abdou, and et al. Calibration and characterization of the icecube photomultiplier tube. *Nuclear Instruments and Methods in Physics Research Section A: Accelerators, Spectrometers, Detectors and Associated Equipment*, 618(1):139–152, 2010.
- [6] M. Ageron et al. ANTARES: the first undersea neutrino telescope. *Nucl. Instrum. Meth. A*, 656:11–38, 2011.

BIBLIOGRAPHY

- [7] Matteo Agostini, Michael Böhmer, Jeff Bosma, Kenneth Clark, Matthias Danninger, Christian Fruck, Roman Gernhäuser, Andreas Gärtner, Darren Grant, Felix Henningsen, and et al. The pacific ocean neutrino experiment. *Nature Astronomy*, 4(10):913–915, Sep 2020.
- [8] E. Andres et al. The AMANDA neutrino telescope: Principle of operation and first results. *Astropart. Phys.*, 13:1–20, 2000.
- [9] J. Babson, B. Barish, R. Becker-Szendy, H. Bradner, R. Cady, J. Clem, S. T. Dye, J. Gaidos, P. Gorham, P. K. F. Grieder, M. Jaworski, T. Kitamura, W. Kropp, J. G. Learned, S. Matsuno, R. March, K. Mitsui, D. O’Connor, Y. Ohashi, A. Okada, V. Peterson, L. Price, F. Reines, A. Roberts, C. Roos, H. Sobel, V. J. Stenger, M. Webster, and C. Wilson. Cosmic-ray muons in the deep ocean. *Phys. Rev. D*, 42:3613–3620, Dec 1990.
- [10] John N. Bahcall. Solar neutrinos. i. theoretical. *Phys. Rev. Lett.*, 12:300–302, Mar 1964.
- [11] A. Bellerive, J.R. Klein, A.B. McDonald, A.J. Noble, and A.W.P. Poon. The sudbury neutrino observatory. *Nuclear Physics B*, 908:30–51, Jul 2016.
- [12] G. Bellini, A. Ianni, L. Ludhova, F. Mantovani, and W.F. McDonough. Geo-neutrinos. *Progress in Particle and Nuclear Physics*, 73:1–34, Nov 2013.
- [13] I. A. Belolaptikov et al. The Baikal underwater neutrino telescope: Design, performance and first results. *Astropart. Phys.*, 7:263–282, 1997.
- [14] S. Bhattacharai, D. M. Mei, and M. S. Raut. Low-energy solar neutrino detection utilizing advanced germanium detectors, 2021.

BIBLIOGRAPHY

- [15] M. Boehmer, J. Bosma, D. Brussow, L. Farmer, C. Fruck, R. Gernhäuser, A. Gärtner, D. Grant, F. Henningsen, S. Hiller, and et al. Straw (strings for absorption length in water): pathfinder for a neutrino telescope in the deep pacific ocean. *Journal of Instrumentation*, 14(02):P02013–P02013, Feb 2019.
- [16] Federica Bradascio. Search for high-energy neutrinos from agn cores, 2019.
- [17] Laurie M. Brown. The idea of the neutrino. *Physics Today*, 31(9):23–28, September 1978.
- [18] D. Casper, R. Becker-Szendy, C. B. Bratton, D. R. Cady, R. Claus, S. T. Dye, W. Gajewski, M. Goldhaber, T. J. Haines, P. G. Halverson, T. W. Jones, D. Kielczewska, W. R. Kropp, J. G. Learned, J. M. LoSecco, C. McGrew, S. Matsuno, J. Matthews, M. S. Mudan, L. Price, F. Reines, J. Schultz, D. Sinclair, H. W. Sobel, J. L. Stone, L. R. Sulak, R. Svoboda, G. Thornton, and J. C. van der Velde. Measurement of atmospheric neutrino composition with the imb-3 detector. *Phys. Rev. Lett.*, 66:2561–2564, May 1991.
- [19] P A Cherenkov. Dokl. Akad. Nauk SSSR. [*Comptes Rendus Acad. Sciences USSR* 2 451 (1934)], 2(451), 1934.
- [20] Lew Classen, Alexander Kappes, and Timo Karg. A multi-pmt optical module for the icecube upgrade, 2019.
- [21] Y. H. Dai and Y. Yuan. A nonlinear conjugate gradient method with a strong global convergence property. *SIAM J. Optim.*, 10:177–182, 1999.

BIBLIOGRAPHY

- [22] G. Danby, J. Gaillard, K. Goulian, L. Lederman, N. Mistry, M. Schwartz, and J. Steinberger. Observation of high-energy neutrino reactions and the existence of two kinds of neutrinos. *Physical Review Letters*, 9:36–44, 1962.
- [23] Raymond Davis. Solar neutrinos. ii. experimental. *Phys. Rev. Lett.*, 12:303–305, Mar 1964.
- [24] W.J. Marciano E. Blucher. The cabibbo angle and ckm unitarity. <https://pdg.lbl.gov/2020/reviews/rpp2020-rev-vud-vus.pdf>.
- [25] Justin Evans. The minos experiment: results and prospects, 2013.
- [26] Thomas K. Gaisser. Atmospheric neutrinos, 2019.
- [27] V. L. Ginzburg. Radiation from uniformly moving sources (vavilov-cherenkov effect, transition radiation, and some other phenomena). *Acoustical Physics*, 51, Feb 2005.
- [28] Carlotta Giusti and Martin V Ivanov. Neutral current neutrino-nucleus scattering: theory. *Journal of Physics G: Nuclear and Particle Physics*, 47(2):024001, Jan 2020.
- [29] Particle Data Group and et al. Zyla. Review of Particle Physics. *Progress of Theoretical and Experimental Physics*, 2020(8), 08 2020. 083C01.
- [30] Mike Guidry and Jay Billings. A basic introduction to the physics of solar neutrinos, 2018.
- [31] HAMAMATSU. *PHOTOMULTIPLIER TUBES: Basics and Applications*. HAMAMATSU, 2009.

BIBLIOGRAPHY

- [32] K. S. Hirata et al. Observation of a small atmospheric muon-neutrino / electron-neutrino ratio in Kamiokande. *Phys. Lett. B*, 280:146–152, 1992.
- [33] K. S. Hirata, T. Kajita, T. Kifune, K. Kihara, M. Nakahata, K. Nakamura, S. Ohara, Y. Oyama, N. Sato, M. Takita, Y. Totsuka, Y. Yaginuma, M. Mori, A. Suzuki, K. Takahashi, T. Tanimori, M. Yamada, M. Koshiba, T. Suda, K. Miyano, H. Miyata, H. Takei, K. Kaneyuki, H. Nagashima, Y. Suzuki, E. W. Beier, L. R. Feldscher, E. D. Frank, W. Frati, S. B. Kim, A. K. Mann, F. M. Newcomer, R. Van Berg, and W. Zhang. Observation of ${}^8\text{B}$ solar neutrinos in the kamiokande-ii detector. *Phys. Rev. Lett.*, 63:16–19, Jul 1989.
- [34] Jurkovic, M., Abraham, K., Holzapfel, K., Krings, K., Resconi, E., and Veenkamp, J. A precision optical calibration module (pocam) for icecube-gen2. *EPJ Web of Conferences*, 116:06001, 2016.
- [35] A. Karle. Icecube, 2010.
- [36] Spencer R. Klein. Icecube: A cubic kilometer radiation detector. *IEEE Transactions on Nuclear Science*, 56(3):1141–1147, Jun 2009.
- [37] K. Kodama, N. Ushida, C. Andreopoulos, N. Saoulidou, G. Tzanakos, P. Yager, B. Baller, D. Boehnlein, W. Freeman, B. Lundberg, and et al. Observation of tau neutrino interactions. *Physics Letters B*, 504(3):218–224, Apr 2001.
- [38] S KOPP. Accelerator neutrino beams. *Physics Reports*, 439(3):101–159, Feb 2007.
- [39] A Kumar, A M Vinod Kumar, Abhik Jash, Ajit K Mohanty, Aleena Chacko, Ali Ajmi, Ambar Ghosal, Amina Khatun, Amitava Raychaudhuri, Amol Dighe, and

BIBLIOGRAPHY

- et al. Invited review: Physics potential of the ical detector at the india-based neutrino observatory (ino). *Pramana*, 88(5), Apr 2017.
- [40] Andrew John Lowe. Neutrino physics & the solar neutrino problem, 2009.
- [41] B.K. Lubsandorzhiev. On the history of photomultiplier tube invention. *Nuclear Instruments and Methods in Physics Research Section A: Accelerators, Spectrometers, Detectors and Associated Equipment*, 567(1):236–238, 2006. Proceedings of the 4th International Conference on New Developments in Photodetection.
- [42] C. Lunardini and A.Yu. Smirnov. Supernova neutrinos: Earth matter effects and neutrino mass spectrum. *Nuclear Physics B*, 616(1-2):307–348, Nov 2001.
- [43] Ziro Maki, Masami Nakagawa, and Shoichi Sakata. Remarks on the Unified Model of Elementary Particles. *Progress of Theoretical Physics*, 28(5):870–880, 11 1962.
- [44] A Margiotta. A parameterisation of single and multiple muons in the deep water or ice. *Journal of Physics: Conference Series*, 39:435–437, May 2006.
- [45] Séverine Martini and Steven H. D. Haddock. Quantification of bioluminescence from the surface to the deep sea demonstrates its predominance as an ecological trait. *Scientific Reports*, 7, 04 2017.
- [46] Mikheyev, Smirnov S. P., and A. Yu. Resonant amplification of ν oscillations in matter and solar-neutrino spectroscopy. *Il Nuovo Cimento C*, 9, Jan 1986.
- [47] J. Nelder and R. Mead. A simplex method for function minimization. *Comput. J.*, 7:308–313, 1965.

BIBLIOGRAPHY

- [48] William H. Press and Saul A. Teukolsky. Savitzky-golay smoothing filters. *Computers in Physics*, 4(6):669–672, 1990.
- [49] Xin Qian and Jen-Chieh Peng. Physics with reactor neutrinos. *Reports on Progress in Physics*, 82(3):036201, Feb 2019.
- [50] F. Reines, C. L. Cowan, F. B. Harrison, A. D. McGuire, and H. W. Kruse. Detection of the free antineutrino. *Phys. Rev.*, 117:159–173, Jan 1960.
- [51] Byron P. Roe. *Probability and Statistics in the Physical Sciences*. Springer International Publishing, 2001.
- [52] Kai Schatto. *Stacked searches for high-energy neutrinos from blazars with Ice-Cube*. PhD thesis, Mainz U., 6 2014.
- [53] Arun Kumar Soma and Henry Tsz-King Wong. Germanium detectors with sub-keV sensitivities for neutrino and dark matter physics. *J. Phys. Conf. Ser.*, 606(1):012011, 2015.
- [54] I E Tamm and I M Frank. Dokl. Akad. Nauk SSSR. [*Comptes Rendus Acad. Sciences USSR 14 107 (1937)*], 14(107), 1937.
- [55] N. van Eijndhoven, O. Fadiran, and G. Japaridze. Implementation of a gauss convoluted pandel pdf for track reconstruction in neutrino telescopes. *Astroparticle Physics*, 28(4-5):456–462, Dec 2007.
- [56] S I Vavilov. Dokl. Akad. Nauk SSSR. [*Comptes Rendus Acad. Sciences USSR 2 457 (1934)*], 2(457), 1934.

BIBLIOGRAPHY

- [57] D. Vignaud. The gallex solar neutrino experiment. *Nuclear Physics B - Proceedings Supplements*, 60(3):20–29, 1998.
- [58] L. V. Volkova. Energy Spectra and Angular Distributions of Atmospheric Neutrinos. *Sov. J. Nucl. Phys.*, 31:784–790, 1980.
- [59] Christopher W. Walter. The super-kamiokande experiment. *Neutrino Oscillations*, page 19–43, Mar 2008.
- [60] Edith Widder. Bioluminescence in the ocean: Origins of biological, chemical, and ecological diversity. *Science (New York, N.Y.)*, 328:704–8, 05 2010.